Study of Spatial Structure of Squeezed Vacuum Field

Mi Zhang

Shangqiu, Henan, China

Master of Science, College of William & Mary, 2013
Bachelor of Science, Fudan University, 2011

A Dissertation presented to the Graduate Faculty
of The College of William & Mary in Candidacy for the Degree of
Doctor of Philosophy

Department of Physics

College of William & Mary
May 2017

©2017
Mi Zhang
All rights reserved.

APPROVAL PAGE

This Dissertation is submitted in partial fulfillment of
the requirements for the degree of

Doctor of Philosophy

Mi Zhang

Approved by the Committee, March, 2017

Committee Chair
Assistant Professor Eugeniy E. Mikhailov, Physics
College of William & Mary

Associate Professor Seth Aubin, Physics
College of William & Mary

Associate Professor Irina Novikova, Physics
College of William & Mary

Professor John B. Delos, Physics
College of William & Mary

Assistant Professor Alberto M. Marino, Physics
University of Oklahoma

ABSTRACT

Squeezed states of light, with field fluctuations smaller than the coherent state fluctuations (or shot noise), are used for improving accuracy of quantum-noise limited measurements, like the detection of gravitational waves. They are also essential resources for quantum information transfer protocols. We studied a squeezed vacuum field generated in hot Rb vapor via the polarization self-rotation effect. We studied the mode structure of the squeezed field by spatially-masking the laser beam after its interaction with the Rb atomic vapor. From analysis of the data we developed a multi-mode theory to simulate the mode composition of the squeezed vacuum field. Our experiments showed that the amount of observed squeezing may be limited by the complex mode structure due to the excitement of higher order spatial modes during the nonlinear atom-light interaction. We demonstrated that optimization of the spatial profile of the beam led to higher detected squeezing. Our studies are useful for enhancing precision metrology and quantum memory applications.

TABLE OF CONTENTS

ACKNOWLEDGMENTS

After arriving in the US in 2011, I started to work in in the Group of Professor Eugeniy E. Mikhailov and study the nature of squeezed fields. He supported me through the six years of my Ph.D. life and trained me from an apprentice researcher into a Ph.D.. I am really grateful to be working with him, a learned, nice and funny advisor. In the meantime, I also got a lot of advices and help from Professor Irina Novikova, who works in the same group. I learned how to do optics experiments in the lab of Professor Yanhong Xiao in Fudan University. She is the very first person who initiated my interest in quantum optics. I really appreciated the knowledge and scientific method these people have taught me.

I enjoyed working in this lab not only because of my advisors are nice and helpful, my fellow Ph.D. students, Matt Simons, Travis Horrom, Gleb Romanov, Ellie Radue, Nik Prajapati and Demetrious Kutzke are also friendly and fun. Travis offered me quite a lot of help on the squeezing project, Matt had the best coffee and beer in the whole department, with Gleb I practiced my spoken English by expressing how we liked or disliked the Apple products, Ellie and I always shared the room when we were out on a conference, Nik made the lab a much happier place with laughters and Demetry did the proof reading of my first thesis draft("eye-bleeding", according to my advisor). I also want to thank some undergrads who have worked in the lab, Joseph Soultanis, Jesse Evans, Owen Wolfe and Melissa Guidry, for the help they have provided in the experiments. In the collaboration with theorists from Louisiana State University, I learned quite a lot from Professor Jon Dowling and his students Nick Lanning and Zhihao Xiao.

I would also thank the department of physics and the committee members for the help and resources they provided. Professor Aubin and Professor Delos have been my annual review committee members since five years ago. Professor Marino travelled all the way down to Williamsburg to attend my defence.

Last but not least, I would express my gratitude to my friends here in Williamsburg, Zhen, Hao, Du, Zhiying and Shuangli, for the time we spent together. My family, especially Mom, Dad and my sister Summer, gave me quite a lot of support in my Ph.D. life. Also, thanks to Max and Taro for making the world a better place, may your tails be forever wagging.

Dedicated to my sister Summer.

CHAPTER 1

Introduction

Squeezed states of light field are non-classical states, in which the observables have some uncertainties lower than that in the "normal" coherent states. Uncertainties or noise in the coherent states are often denoted as the shot noise, or the standard quantum limit. Therefore, squeezed states are often adopted to improve the precision in quantum noise limited measurements utilizing optical fields.

However, the amount of noise suppression or squeezing one can detect is often limited by many experimental factors. An important factor is the complicated spatial structure of the optical field generated in the non-linear interaction between the input optical field and the medium. This complexity, as we will discuss in Chapter 5, degrades the detected amount of squeezing.

In this dissertation, we focus on the spatial properties of a squeezed vacuum field. Studying this topic promises a better understanding of how the medium distorts the

squeezed field, and how we can find means to avoid the complex structure generation. With such knowledge it is possible to achieve higher squeezing and thus improve the measurement precision in many applications, such as magnetometers and spectroscopy.

In this chapter, we introduce the basics of noise in optical systems, and why the squeezed field has lower quantum noise. We address the development of the study on squeezed states, as well as some different techniques to generate them. We also discuss some applications of the squeezed states, and finally we review the outline of this dissertation.

1.1 Sources of noise

Any experiment suffers from uncertainties or noise that originate from a variety of sources. In experiments related to optical and atomic physics, noise originated from both classical and quantum sources. Classical noise includes vibration of the apparatus, laser frequency drifting, thermal drift and intensity fluctuation of the laser. All noise of these types can be suppressed to some degree if we have proper experimental control over the system.

However, there is intrinsic noise, which comes from the quantum nature of the optical field and cannot be eliminated or reduced by any classical means. This is the quantum noise of the system. The Heisenberg uncertainty principle states that for a pair of conjugate variables, the product of their uncertainties must be no less than a certain value. A most well-known example of this principle is, a particle's position and momentum cannot be determined simultaneously to arbitrary precision, i.e.$\Delta x \Delta p \geq \hbar/2$. For an optical field,

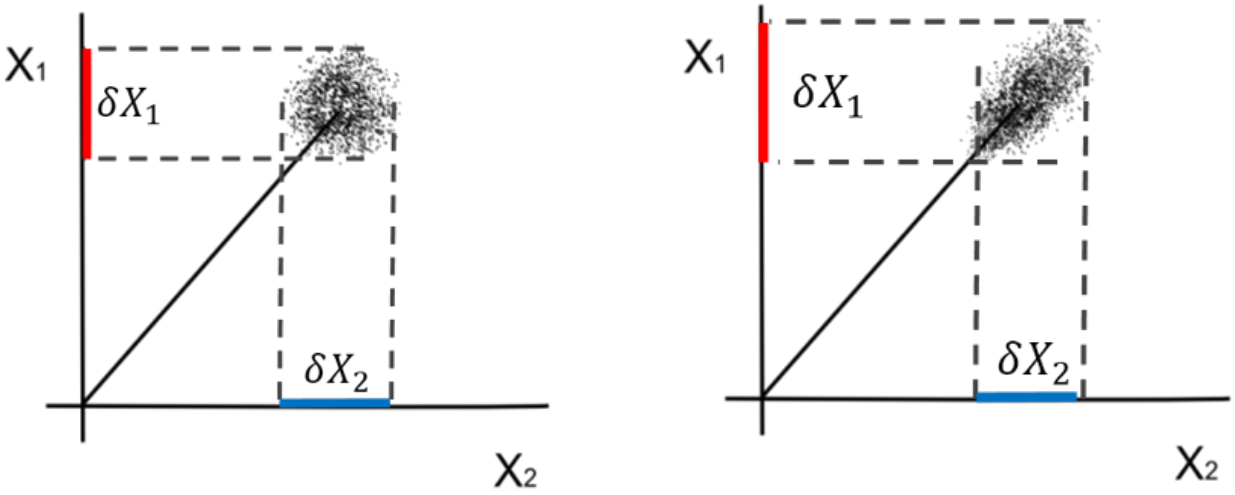

FIG. 1.1: The dashed area represents the product of the uncertainties of the state. Horizontal and vertical axes represent the quadrature that one uses to describe a field, noted as X_1 and X_2; we will define them later in Chapter 2. The projections of the uncertainty area (red and blue lines) are the fluctuations in these quadratures. In a coherent field, the length of the red and blue lines are the same, meaning that the fluctuations are the same for both quadratures. In a squeezed field, the red is longer and the blue is shorter, indicating a modified field distribution.

the pair of non-commuting observables is the phase and the amplitude. The uncertainty principle, therefore, limits the minimum product of the uncertainties in the amplitude and the phase. The optical field in a coherent state has this minimum uncertainty product, and in such states the uncertainties of the two observables are equal. However, with specific techniques, we can decrease the uncertainty in one of these observables and increase the uncertainty in the other as compensation without violating the Heisenberg uncertainty principle. Such states with fluctuations suppressed in a certain observable are called squeezed states.

1.2 Squeezed state

In some measurements, when we have to deal with weak signals, the quantum noise may become a major limitation. Under these conditions, squeezed states can be used to reduce the quantum noise. In Fig. 1.1, we compare the field distribution of a coherent state and a phase-squeezed state. The coherent state has equal uncertainties in phase and amplitude, or as is shown in the left figure, equal projections in horizontal and vertical axes. We will talk about this formalism later in Chapter 2. For now we only consider phase and amplitude. In the squeezed state shown in the right of Fig. 1.1, the fluctuation in the phase is suppressed, with the fluctuation in the amplitude increased as compensation. Measurements utilizing a phase-squeezed field, such as in an interferometer, can benefit from better precision. Similarly, when the field features suppressed noise in the amplitude and higher phase noise, it can be used in quantum imaging for higher resolution. In the ideal squeezed state, the product of the two uncertainties is the same as that of a coherent state. However, in most experimental conditions, the squeezed state has an enlarged product of uncertainties.

1.3 History of squeezing development

The theory of squeezing was first introduced in the 1960s, immediately following the invention of the laser. In the past decades, researchers have been working on both getting higher squeezing and utilizing new methods to achieve squeezing. In the 1980s, D. F.

Walls published a review article [1] in which he described a state of light that has unequal amount of uncertainties in the two conjugate variables. Caves and Schumaker later gave a two-photon formalism to describe the squeezed field [2]. The search for squeezed states was initialized since then, and the first demonstration of squeezing was reported by Slusher [3], using a four-wave-mixing (4WM) procedure in sodium vapor. Shortly after, Shelby also demonstrated a squeezed state in a fiber ring cavity [4, 5, 6] utilizing non-degenerate 4WM. In the same period, Kimble et al. were able to produce a squeezed state utilizing parametric down conversion in a nonlinear crystal [7, 8], as well as in a cavity quantum electrodynamics system with Na[9]. Other than simply generating a squeezed field, they also proved that replacing the vacuum port of the interferometer with squeezed vacuum can improve the measurement accuracy [10]. To date, nonlinear crystals are still an important medium for squeezing generation. The best squeezing so far is reported by Schnabel utilizing optical parametric oscillation (OPO) in such medium in a ring cavity [11] . They had a direct detection of -15 dB of squeezing. Instead of manipulating the light field from a commercial laser, the Yamamoto Group modulated the current of a semiconductor laser directly and produced an amplitude-squeezed light [12, 13].

More recently, a method that utilizes the polarization self-rotation (PSR) effect in an atomic vapor was proposed [14, 15] for generating a squeezed vacuum field. Experimental realization by Lvovsky soon followed [16]. Such an experimental apparatus excels in its simplicity and low cost, and it produces reasonable noise suppression. A series of squeezed vacuum generation results has been observed in this configuration [16, 17, 18, 19, 20]. So

far, the highest squeezing generated in this setup is -3 dB by Lezama [18], compared to a theoretical prediction of -8 dB in [14].

The spatial distribution of a squeezed field is also a topic that attracts lots of interest. As early as 1993, Gatti calculated the spatial spectrum of a squeezed field generated in a degenerate parametric oscillation [21]. The Lett group has studied the spatial structure of the squeezed field generated in a 4WM process [22, 23, 24].

1.4 Applications of squeezed field

Lowering the uncertainties in optical measurements is one of the most important applications of squeezed fields. As is suggested by Caves and Schumaker [2], a squeezed field can be used to replace the coherent vacuum in the empty port of an optical interferometer and improve measurement accuracy. One of the most precise interferometers in the world is the Laser Interferometric Gravitational-Wave Observatory (LIGO), which has successfully detected gravitational waves in 2015. In a few test runs, a squeezed vacuum field has been proven to increase its detection sensitivity [25, 26].

The use of squeezed fields to improve measurement accuracy is not limited to interferometers. Theoretically, all measurements utilizing optical fields can benefit from amplitude squeezed fields, e.g., magnetometers [20, 27, 28], spectroscopy[29] and quantum tomography[30].

With the development of quantum information in recent years, squeezed fields have become an important source for photon pair generation [31, 32, 33, 34, 35]. They are also

used for improving the signal to noise ratio in information teleportation [36]. In quantum imaging and sensing, the resolution can be pushed beyond the standard quantum limit with a squeezed state [20, 27, 28, 37, 38, 39, 40, 41].

1.5 Outline of the dissertation

This dissertation is arranged in the following manner. In Chapter 2, starting from Maxwell's equations, we find wave function solutions and the possible spatial modes in the second chapter. We quantize the field by replacing the coordinate and momentum with corresponding operators, and we introduce the quadrature operators to describe the field. We then review the squeezed field and the coherent field, as well as the definition of squeezing. In the third chapter we introduce the detection scheme used to observe squeezing. We present the experimental setup and study the parameters that can be optimized to observe the theoretically predicted value of squeezing in our system.

In the fourth chapter we show our results on the detected noise suppression. I investigate the dependence of squeezing on the self-focussing effect and reveal that there is no direct correlation between them.

In Chapter 5 we use different spatial masks on the output beams to demonstrate that the spatial profile of the beams, both the squeezed vacuum and the local oscillator, are not in the fundamental Gaussian mode. We develop a theory on how the atomic system changes the beam shape.

In Chapter 6, to eliminate or weaken such beam distortion in the cell, we build a

multi-pass setup and are able to generate improved squeezing. We demonstrate that the optical depth is not the only parameter that determines the squeezing. We also show in this chapter that a pump beam modified by a cell can produce higher squeezing. In Chapter 7, we demonstrate improved squeezing result by using a pump beam that has been spatially optimized with a spatial light modulator (SLM). Also, we try to change the spatial profile of the local oscillator that amplifies the squeezed vacuum, but this experiment does not exhibit any improvement.

With a high-precision camera in Chapter 8 we directly monitor the spatial distribution of noise in the beams. The change of normalized noise in a beam after interaction with atoms elucidate the spatial structure.

Chapter 9 is the summary of these projects.

CHAPTER 2

Theory of Squeezed State Generation

In this chapter we introduce some basic concepts to understand our squeezing experiment. We start from the quantization of electromagnetic field, obtain the annihilation and creation operators and the quadrature operators. Then we discuss the most commonly achieved state of the light field – the coherent state, which has equal fluctuations in both quadratures. Differing from the coherent state, the squeezed state has different statistics in quadrature fluctuations and is a more interesting state to deal with. Last we will describe the technique used to generate a squeezed vacuum field, the theoretically predicted value of the noise suppression, and the factors limiting us from getting the expected value.

2.1 Single mode solution of electromagnetic field

We start with the Maxwell equations to describe the light field propagation in free space.

$$\nabla \cdot \mathbf{E} = \frac{\rho}{\epsilon_0} \tag{2.1}$$

$$\nabla \cdot \mathbf{B} = 0 \tag{2.2}$$

$$\nabla \times \mathbf{E} = -\frac{\partial \mathbf{B}}{\partial t} \tag{2.3}$$

$$\nabla \times \mathbf{B} = \mu_0 \epsilon_0 \frac{\partial \mathbf{E}}{\partial t} + \mu_0 \mathbf{J} \tag{2.4}$$

where $\mathbf{E}$ and $\mathbf{B}$ are the magnitude of the electric and magnetic fields respectively, ρ is the charge density, and $\mathbf{J}$ is the current flux density. ϵ_0 and μ_0 are the electric permittivity and magnetic permeability of vacuum. In free space, both ρ and $\mathbf{J}$ are zero. We apply Eq. 2.3 to Eq. 2.4 and take the curl.

$$\nabla \times (\nabla \times \mathbf{E}) = -\mu_0 \epsilon_0 \frac{\partial^2 \mathbf{E}}{\partial t^2} \tag{2.5}$$

$$\nabla^2 \mathbf{E} + \mu_0 \epsilon_0 \frac{\partial^2 \mathbf{E}}{\partial t^2} = 0. \tag{2.6}$$

In a cavity resonator, a possible solution to this equation takes the form of

$$E_x(z,t) = \sqrt{\frac{2\omega^2}{V\epsilon_0}} q(t) \sin(kz), \tag{2.7}$$

where the wave vector k is defined as $k = \omega/c$, ω is the frequency of the field, V is the volume. Similarly, a possible solution for the magnetic field is

$$B_y(z,t) = \frac{\mu_0 \epsilon_0}{k} \sqrt{\frac{2\omega^2}{V\epsilon_0}} \dot{q}(t) \cos(kz). \tag{2.8}$$

We define the momentum to be $p(t) = \dot{q}(t)$.

2.2 Spatial modes and field distribution

If we use the paraxial approximation for a slowly-varying optical field travelling in the z-direction as is in the paraxial Helmholtz equations.

$$\left(\nabla^2 + k^2\right) u = 0 \tag{2.9}$$

Here u is the amplitude of the field. The solutions can be expressed as combinations of Hermite-Gaussian modes or Laguerre-Gaussian modes. Usually in a Cartesian coordinates, the Hermite-Gaussian (HG) modes are used for convenience. Meanwhile in cylindrical coordinates, Laguerre-Gaussian (LG) modes excel in their cylindrical symmetry.

In the Hermite-Gaussian basis, the amplitude distribution of the modes is

$$\begin{aligned} u_{l,m}(x,y,z) = u_0 \frac{w_0}{w(z)} H_l\left(\frac{\sqrt{2}x}{w(z)}\right) H_m\left(\frac{\sqrt{2}y}{w(z)}\right) \exp\left(-\frac{x^2+y^2}{w^2(z)}\right) \times \\ \exp\left[-i\frac{k(x^2+y^2)}{2R(z)}\right] \exp(-ikz) \exp\left[i(|l|+|m|+1)\arctan(z/z_R)\right], \end{aligned} \tag{2.10}$$

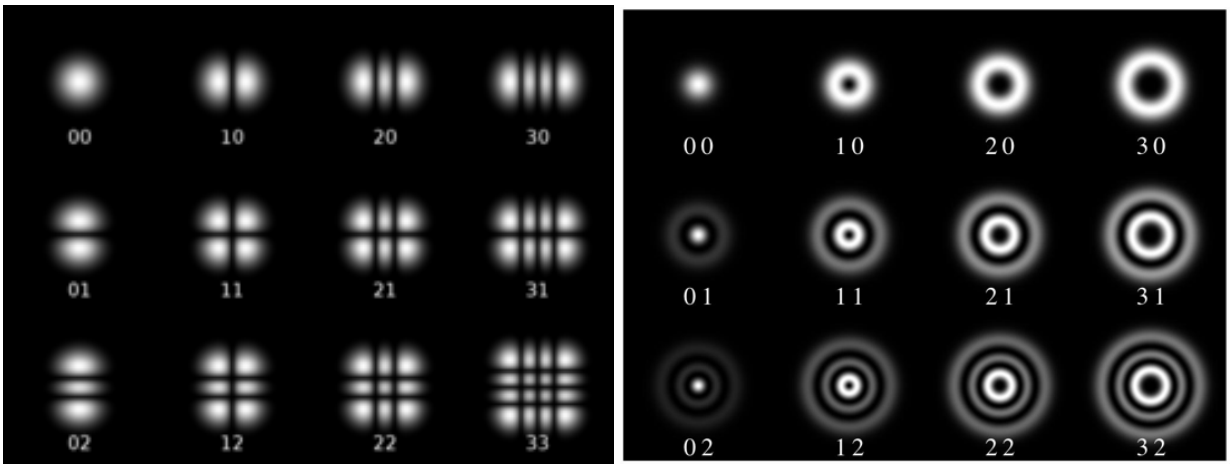

FIG. 2.1: Some examples of higher order Hermite-Gaussian (left) and Laguerre-Gaussian (right) modes. Figures are taken from Wikipedia page - Gaussian beam.

where l and m are the orders of HG modes. They each represents how many knots there are in the x- or the y-direction. H_l are the Hermite polynomials of the lth order. R is the radius of curvature, defined as

$$R(z) = z\left[1 + \left(\frac{z_R}{z}\right)^2\right] \tag{2.11}$$

z_R is called Rayleigh range, we will talk about it later. The expression of the field distribution for Laguerre-Gaussian modes is

$$\begin{aligned} u_{l,p}(r,\phi,z) = \frac{C_{lp}^{LG}}{w(z)}\left(\frac{r\sqrt{2}}{w(z)}\right)^{|l|}\exp\left(-\frac{r^2}{w^2(z)}\right)L_p^{|l|}\left(\frac{2r^2}{w^2(z)}\right) \\ \exp\left(-ik\frac{r^2}{2R(z)}\right)\exp(il\phi)\exp\left[i(2p+|l|+1)\arctan(z/z_R)\right] \end{aligned} \tag{2.12}$$

where l is the radial index and p is the azimuthal index. They are used to note the order of corresponding LG mode. C_{lp}^{LG} is a normalization constant. $L_p^{|l|}$ are the generalized

Laguerre polynomials.

2.2.1 Gaussian mode

The lowest-order modes of HG and LG distribution of an optical field are the same. The expression of cross section field amplitude is (we use the electric field for simplicity)

$$E(r,z) = E_0(z)\, e^{-\frac{r^2}{w(z)^2}} \tag{2.13}$$

In the equation above, $E(r,z)$ is the field amplitude at a position of z away from the focus and radius r from the axis. The waist $w(z)$ is the radius where the field amplitude falls to $\frac{1}{e}$ of the axial value $E_0(z)$. At a position z on the optical axis, the beam waist w is described by

$$w(z) = w_0\sqrt{1+\left(\frac{z}{z_R}\right)^2}, \tag{2.14}$$

where w_0 is the minimum beam size at focus and z_R is a parameter called Rayleigh range.

$$z_R = \frac{\pi w_0^2}{\lambda} \tag{2.15}$$

2.2.2 Gouy Phase

The phase factor $\exp\left[i(|l|+|m|+1)\arctan(z/z_R)\right]$ in Eq. 2.10 and $\exp\left[i(2p+|l|+1)\arctan(z/z_R)\right.$ in Eq. 2.12 are referred to as the Gouy phase. Gouy phase has a π shift around the focus of a propagating beam, Fig. 2.2 (b) shows the phase shift in a Gaussian beam.

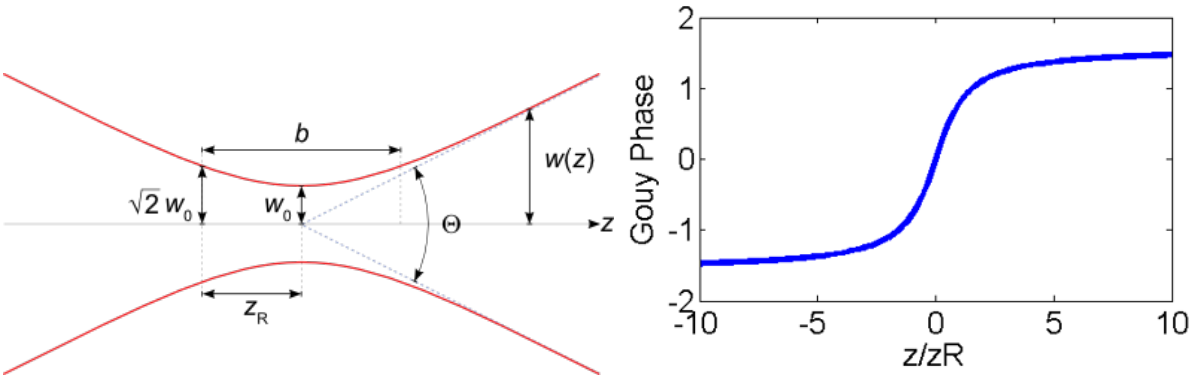

FIG. 2.2: (a) a Gaussian beam width profile, taken from Wikipedia page - Gaussian beam. (b) Gouy phase change of the Gaussian beam across the waist.

2.3 Quantization of the electromagnetic field

Now let us focus back on the plane wave. To quantize the position and momentum, we replace them with a pair of non-commuting operators, $\hat{q}$ and $\hat{p}$., which obey the commutation relation given by

$$[\hat{q}, \hat{p}] = i\hbar\hat{I}. \tag{2.16}$$

Instead of $\hat{q}$ and $\hat{p}$, we introduce another pair of operators here,

$$\hat{a} = \frac{1}{\sqrt{2\hbar\omega}} \left(\omega\hat{q} + i\hat{p}\right), \tag{2.17}$$

and

$$\hat{a}^\dagger = \frac{1}{\sqrt{2\hbar\omega}} \left(\omega\hat{q} - i\hat{p}\right). \tag{2.18}$$

These are called the annihilation and creation operators, respectively, corresponding to annihilating or adding one photon into the system. The annihilation and creation operators

are non-commuting as well

$$\left[\hat{a}, \hat{a}^{\dagger}\right] = 1. \tag{2.19}$$

Classically the Hamiltonian of the field takes the form of

$$H = \frac{1}{2} \int dV \left[\epsilon_0 E^2 + \frac{1}{\mu_0} B^2\right]. \tag{2.20}$$

We can now refer to the system energy as

$$\begin{aligned} \hat{H} &= \frac{1}{2}\left(p^2 + \omega^2 q^2\right) \\ &= \hbar\omega \left(\hat{a}^{\dagger}\hat{a} + \frac{1}{2}\right). \end{aligned} \tag{2.21}$$

The photon number operator for the system is

$$\hat{n} = \hat{a}^{\dagger}\hat{a}. \tag{2.22}$$

Utilizing the previous results, we can write the field in the quantized form

$$\hat{E} = \epsilon_0 \left(\hat{a}e^{-i\omega t} + \hat{a}^{\dagger}e^{i\omega t}\right) \sin\left(kz\right), \tag{2.23}$$

where all quantum behaviors of the field is encapsulated in the terms in parenthesis, while the field is still modified by a classical profile given by the sinusoidal term. Lastly we use

a pair of quadrature operators to represent the field. They are defined as

$$\hat{X}_1 = \frac{1}{2}\left(\hat{a} + \hat{a}^\dagger\right), \tag{2.24}$$

and

$$\hat{X}_2 = \frac{1}{2i}\left(\hat{a} - \hat{a}^\dagger\right). \tag{2.25}$$

Clearly Eq. 2.23 can be written in the following form

$$\hat{E}_x(t) = 2\epsilon_0 \sin(kz)\left[\hat{X}_1 \cos(\omega t) + i\hat{X}_2 \sin(\omega t)\right]. \tag{2.26}$$

Now we have arrived at the expression of quantized electromagnetic field, presented in quadrature operators.

2.4 Coherent state

A straightforward description of the field is number states (also known as Fock states). They are denoted as the energy eigenstate of the single mode field with energy eigenvalue E_n. By definition, such states have well defined photon numbers but non-well defined phases.

$$\hat{H}|n\rangle = \hbar\omega\left(\hat{a}^\dagger\hat{a} + \frac{1}{2}\right)|n\rangle = E_n|n\rangle. \tag{2.27}$$

The photon number is simply

$$\langle n|\hat{n}|n\rangle = n. \tag{2.28}$$

When the annihilation or the creation operators act on number states, we expect to see a decrease or increase of the photon number. Observe that

$$\hat{a}|n\rangle = \sqrt{n}|n-1\rangle, \tag{2.29}$$

and

$$\hat{a}^{\dagger}|n\rangle = \sqrt{n+1}|n+1\rangle. \tag{2.30}$$

When it comes to the state where no photon is present, we define a vacuum state as

$$\hat{a}|0\rangle = 0. \tag{2.31}$$

Note that in vacuum state the photon number is zero.

In reality, we have not yet found a way to achieve such a pure number state. The most widely used field is a coherent state, which is the state of the light field generated by most manufacturers' lasers. The eigenstate of the annihilation operator is a coherent state.

$$\hat{a}|\alpha\rangle = \alpha|\alpha\rangle. \tag{2.32}$$

It can be described as a displacement from a vacuum state by the displacement operator

$$|\alpha\rangle = \hat{D}\left(\alpha\right)|0\rangle. \tag{2.33}$$

$\hat{D}(\alpha)$ is the displacement operator defined by

$$\hat{D}(\alpha) = \exp\left(\alpha\hat{a}^{\dagger} - \alpha^{\star}\hat{a}\right). \tag{2.34}$$

In such a state, the fluctuations of $\hat{X}_1$ and $\hat{X}_2$ are equal.

$$\langle\alpha|\left(\Delta\hat{X}_1\right)^2|\alpha\rangle = \langle\alpha|\left(\Delta\hat{X}_2\right)^2|\alpha\rangle = \frac{1}{4} \tag{2.35}$$

According to the Heisenberg uncertainty principle, this is the minimum noise one can achieve with "normal" measurements. For any state, the product of these two quadratures must be no less than a certain value.

$$\Delta\hat{X}_1\Delta\hat{X}_2 \geqslant \frac{1}{4} \tag{2.36}$$

In the coherent state, we have $\Delta\hat{X}_1\Delta\hat{X}_2 = \frac{1}{4}$, this is called the standard quantum limit. No classical measurement can get better precision than this limit.

2.5 Squeezed state

Most lasers can easily prepare a light field in a coherent state and a coherent vacuum state. But to depress the fluctuation in a certain quadrature and push noise beyond the

standard quantum limit, we need to apply a squeezing operator.

$$\hat{S}(\xi) = \exp\left[\frac{1}{2}\left(\xi^{\star}\hat{a}^{2} - \xi\hat{a}^{\dagger 2}\right)\right]. \tag{2.37}$$

With a squeezing operator acting on a coherent vacuum, the state becomes

$$|0,\xi\rangle = \hat{S}(\xi)\,|0\rangle, \tag{2.38}$$

which is called a squeezed vacuum state, where ξ is a complex number and

$$\xi = r\exp i\theta \tag{2.39}$$

r is the squeezing parameter and θ the squeezing angle. A more general squeezed state can be achieved by applying the displacement operator onto the squeezed vacuum field

$$|\alpha,\xi\rangle = \hat{D}(\alpha)\,\hat{S}(\xi)\,|0\rangle \tag{2.40}$$

When we take $\theta = 0$, we derive that for such a squeezed field, the fluctuations in the two quadratures are no longer equal.

$$\langle\alpha,\xi|\left(\Delta\hat{X}_{1}\right)^{2}|\alpha,\xi\rangle = \frac{1}{4}\exp(-2r) \tag{2.41}$$

$$\langle\alpha,\xi|\left(\Delta\hat{X}_{2}\right)^{2}|\alpha,\xi\rangle = \frac{1}{4}\exp(2r) \tag{2.42}$$

The photon number in a squeezed state is

$$\langle \alpha, \xi | \hat{n} | \alpha, \xi \rangle = |\alpha|^2 + \sinh^2 r. \tag{2.43}$$

In contrast to a vacuum state, where the photon number is zero, a squeezed vacuum has a photon number of

$$\langle 0, \xi | \hat{n} | 0, \xi \rangle = \sinh^2 r \tag{2.44}$$

2.6 Interaction of light field and atoms

2.6.1 Nonlinear interaction between medium and light

To generate a squeezed field, the most common method is to utilize a non-linear interaction between light field and medium. A medium has nonlinear polarization response to the light field intensity

$$P(t) = \epsilon \left[\chi^{(1)} E(t) + \chi^{(2)} E^2(t) + \chi^{(3)} E^3(t) + ... \right] \tag{2.45}$$

where $\chi^{(i)}$ is the dimensionless ith order susceptibility. Two samples of the interaction Hamiltonians are

$$\hat{H} = i\hbar \left[\alpha \chi^{(2)} \hat{a}^2 - \alpha \chi^{(2)} \hat{a}^{\dagger 2} \right] \tag{2.46}$$

$$\hat{H} = i\hbar \left[\alpha^2 \chi^{(3)} \hat{a}^2 - \alpha^2 \chi^{(3)} \hat{a}^{\dagger 2} \right] \tag{2.47}$$

In Schrodinger's picture, the time-varying state will be evolving in the form of

$$|\varphi(t)\rangle = \exp\left(\frac{i\hat{H}t}{\hbar}\right)|\varphi(0)\rangle \tag{2.48}$$

This equation has same form with Eq. 2.38. Eq 2.46 describe the Hamiltonian in a parametric amplification and Eq 2.47 is the Hamiltonian of a 4WM process or in a Kerr medium.

2.6.2 Polarization self-rotation effect

When atoms are exposed to a time-varying electromagnetic field, in our case a laser beam, there will exist an energy shift induced in the atom energy structure. This shift is proportional to the intensity of the external field, and is called AC Stark effect. The change in energy level in turn generates a change in absorption rate and refraction index of the atomic ensemble as a medium.

When circularly polarized light propagates through a nonlinear medium, in our case an atomic ensemble, the AC Stark effect will generate a modulated refractive index of the medium to the light. Therefore, for elliptically polarized light, the two fields that the medium sees will encounter different path lengths and phase retardation. This generates a change of the field's polarization state in the final output. The rotation angle generated here is

$$\varphi = g\epsilon(0)\, l, \tag{2.49}$$

where g is called a self-rotation parameter that depends on the intrinsic properties of the non-linear medium, the intensity and the frequency of the light. The initial ellipticity of the field is given by $\epsilon(0)$ and l is the length of medium. When it comes to linearly polarized light, the intensities of these two fields are the same. However, when the orthogonal field is coherent vacuum, the vacuum fluctuations in the field serve as the polarization ellipticity. Therefore the time-varying fluctuation will generate a cross-phase modulation, resulting

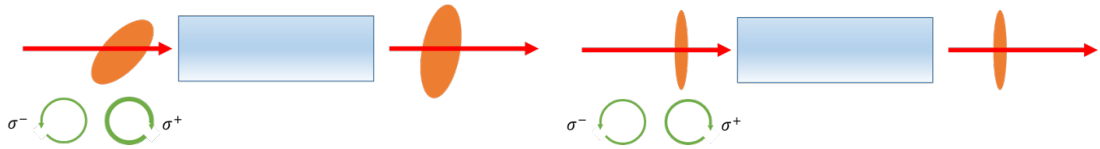

FIG. 2.3: This is a straightforward configuration that shows how the field polarization has been changed through this non-linear medium. Figure on the left shows the rotation in an elliptically polarized field. Figure on the right shows that for a linearly polarized light, the ellipticity does not change.

in a squeezed vacuum field.

2.7 Theoretical prediction of the squeezing level

Previous theory [14] has already made rather complete calculations on how much squeezing we should see in a polarizatoion self rotation(PSR) induced squeezed vacuum field. Here we concisely demonstrate how the squeezed vacuum is generated in the PSR effect. We will start from a classical model and replace the corresponding quantities with operators. If we consider a monochromatic electromagnetic field travelling in the z-direction, the amplitude can be written as

$$E(z,t) = E_x(z,t)\,\hat{x} + E_y(z,t)\,\hat{y}. \tag{2.50}$$

The positive and negative components of the field $E^{\pm}$ are

$$\begin{aligned} E^{+}(z,t) &= \frac{1}{2}\mathcal{E}_x(z)\, e^{i[kz-\omega t+\phi(z)]}\hat{x} + \frac{1}{2}\mathcal{E}_y(z)\, e^{i[kz-\omega t]}\hat{y} \\ E^{-}(z,t) &= \frac{1}{2}\mathcal{E}_x(z)\, e^{-i[kz-\omega t+\phi(z)]}\hat{x} + \frac{1}{2}\mathcal{E}_y(z)\, e^{-i[kz-\omega t]}\hat{y}, \end{aligned} \tag{2.51}$$

where $\mathcal{E}_x(z)$ and $\mathcal{E}_y(z)$ are the real amplitude of the field at the position z, $\phi(z)$ is the relative phase difference between the x and y components. The ellipticity of the system is given by

$$\epsilon = \frac{1}{2}\arcsin\frac{i\left(E_x^- E_y^+ - E_y^- E_x^+\right)}{|E_x|^2 + |E_y|^2}. \tag{2.52}$$

In the limit $E_y \gg E_x$, the ellipticity becomes

$$\epsilon(z) \approx \frac{E_x(z)}{E_y(z)}\sin\phi(z). \tag{2.53}$$

Now let us focus on how the field is rotated by a small angle φ. The rotation matrix is

$$\begin{bmatrix} \cos\varphi & \sin\varphi \\ -\sin\varphi & \cos\varphi \end{bmatrix} \approx \begin{bmatrix} 1 & \varphi \\ -\varphi & 1 \end{bmatrix} \tag{2.54}$$

Referring back to Eq. 2.49 and using the ellipticity in Eq. 2.53, we can calculate the output field after it propagates through a medium of length l. The x-component of the output field is

$$E_x^{+}(l) = \mathcal{E}_x(0)\, e^{i(kl-\omega t)}\left[e^{i\phi(0)} + gl\sin\phi(0)\right] \tag{2.55}$$

Now let's consider the quantized field expressed in annihilation and creation operators.

The phase term $kz - \omega t$ can be replaced with a phase factor χ

$$\hat{E}_x = \frac{1}{2}\mathcal{E}_0 \left[\hat{a}_x(z)\, e^{i\chi} + \hat{a}_x^\dagger(z)\, e^{i\chi}\right]. \tag{2.56}$$

Correspondingly the ellipticity becomes

$$\hat{\epsilon}(z) = \epsilon_0 \frac{\hat{a}_x(z) - \hat{a}_x^\dagger(z)}{2i\mathcal{E}_y(z)} \tag{2.57}$$

. In analogy to Eq. 2.55 the output is

$$\hat{E}_x^+(l) = \frac{1}{2}\left\{\hat{a}_x(0) + \frac{igl}{2}\left[\hat{a}_x^\dagger(0) - \hat{a}_x(0)\right]\right\} e^{i\chi}, \tag{2.58}$$

$$\hat{E}_x(\chi, l) = \frac{\mathcal{E}_0}{2}\hat{a}_x(0)\left(e^{i\chi} - igl\cos\chi\right) + \frac{\mathcal{E}_0}{2}\hat{a}_x^\dagger(0)\left(e^{-i\chi} + igl\cos\chi\right). \tag{2.59}$$

When we have a vacuum field in the x-polarization, the time-average of the amplitude in this polarization yields zero. But the fluctuations are non-zero

$$\begin{aligned}\left\langle \Delta E_x(\chi, l)^2 \right\rangle &= \left\langle \hat{E}_x(\chi, l)^2 \right\rangle - \left\langle \hat{E}_x(\chi, l) \right\rangle^2 \\ &= \left\langle \hat{E}_x(\chi, l)^2 \right\rangle \\ &= \frac{\mathcal{E}_0}{4}\left(1 - 2gl\sin\chi\cos\chi + g^2 l^2\cos^2\chi\right).\end{aligned} \tag{2.60}$$

If we plot the dependence of the fluctuation over the relative phase χ, for maxima or

minima values of the fluctuations, the optimum phase χ_{opt} is

$$\chi_{opt} = \frac{1}{2}\arctan\left(-\frac{2}{gl}\right) + \left(n + \frac{1}{2}\right)\pi, \tag{2.61}$$

where

$$n = 1, 2, 3... \ . \tag{2.62}$$

Considering only when $gl \gg 1$, the minimum fluctuation is approximately

$$\left\langle \left[\Delta E_x\left(\chi_{opt}, l\right)\right]^2 \right\rangle \approx \frac{\mathcal{E}_0^2}{g^2 l^2} \tag{2.63}$$

Now we look at the nonlinear medium that has non-zero absorption. It can be regarded as a beam splitter that replaces the beam with a coherent vacuum. Assuming it is small enough, the squeezed vacuum is attenuated by $e^{-\beta l} \approx 1 - \beta l$. In this case the minimum field fluctuation in Eq. 2.63 becomes

$$\left\langle \left[\Delta E_x\left(\chi_{opt}, l\right)\right]^2 \right\rangle \approx \frac{\mathcal{E}_0^2}{4}\left(\frac{4}{g^2 l^2} + \beta l\right). \tag{2.64}$$

The squeezing parameter, s, is the ratio of the fluctuations in the squeezed quadrature vs. that of the field before it propagates through the medium,

$$s = \sqrt{\frac{\left\langle \left[\Delta E_x\left(\chi_{opt}, l_{opt}\right)\right]^2 \right\rangle}{\mathcal{E}_0^2/4}}. \tag{2.65}$$

With optimization of the relative phase χ and the medium length l, we can find the best noise squeezing parameter to be

$$s = \frac{1}{\sqrt{3}} \left(\frac{g}{\beta} \right)^{\frac{1}{3}} \tag{2.66}$$

In our system where the medium is Rb atom ensemble, we expect a noise depression of -8 dB at least, with the degrading effect of Raman scattering and thermal noise taken into consideration. In reality, the best record of squeezing ever generated in this atomic system is no more than -3 dB as is reported in [18].

CHAPTER 3

Detection of Squeezing

In the previous chapter, we explained the production of a squeezed vacuum field by PSR; now we need to measure the level of noise suppression in this field. The squeezed vacuum field is too weak to be detected by a regular photodetector directly. Here we describe a scheme called homodyne detection for noise detection. The idea of homodyne detection is that the weak fluctuation in the signal field can be amplified by the magnitude of a strong field, so that it is observable at the classical level. In this detection scheme the signal field (in our case, a squeezed vacuum field) is mixed with a local oscillator (a strong field that has the same frequency as the signal and usually comes from the same laser source). Then we present a complete experimental setup and typical noise suppression result. Finally, we demonstrate the dependence of squeezing level's on various experimental parameters.

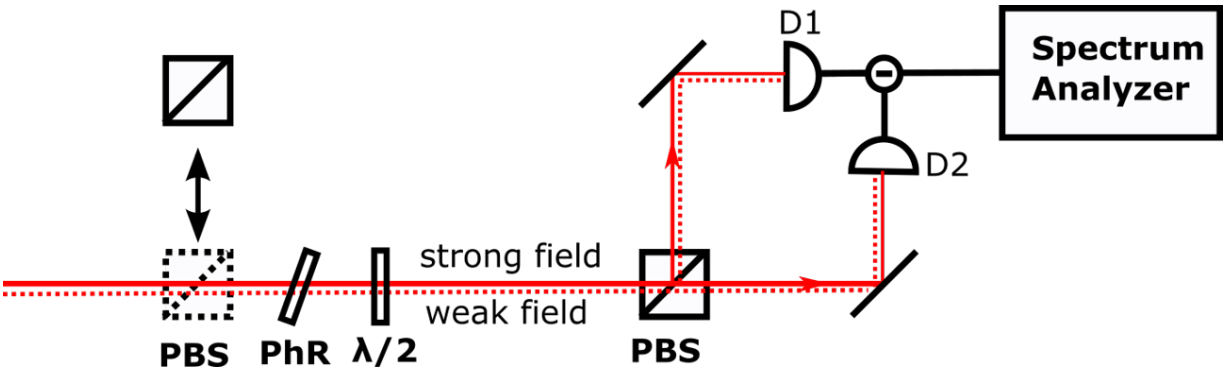

FIG. 3.1: Homodyne detection setup. A weak field (dashed red line, known as the signal field) and a strong field (solid red line) are split on a 50/50 beam splitter. D1 and D2 are two photodetectors. The current detected in the two channels are subtracted from each other. The output of the detection scheme is sent into a spectrum analyzer.

3.1 Homodyne detecting scheme

Assume we have a weak signal field and a strong classical field (referred to as the local oscillator or LO), the amplitudes of these fields are

$$\alpha_s(t) = \alpha_s + \Delta\hat{X}_{1s}(t) + i\Delta\hat{X}_{2s}(t) \tag{3.1}$$

$$\alpha_{LO}(t) = \left[\alpha_{LO} + \Delta\hat{X}_{1LO}(t) + i\Delta\hat{X}_{2LO}(t)\right] e^{i\phi} \tag{3.2}$$

α_s and α_{LO} are the average amplitudes of the signal and the LO fields. The ΔX terms are the quadrature fluctuations. ϕ is the relative phase difference between the strong field and the signal field. The Δ terms in the amplitude represent the quantum fluctuations in the two quadratures we addressed before.

The experimental scheme for homodyne detection is depicted in Fig 3.1. When the two fields are split on the 50/50 beam splitter, one of them encounters a phase shift of π.

In the two channels the fields arriving at the photodetectors are

$$\alpha_{D1} = \sqrt{\frac{1}{2}}\alpha_{LO}(t) + \sqrt{\frac{1}{2}}\alpha_s(t), \tag{3.3}$$

$$\alpha_{D2} = \sqrt{\frac{1}{2}}\alpha_{LO}(t) - \sqrt{\frac{1}{2}}\alpha_s(t). \tag{3.4}$$

In the limit that the amplitude of the strong field is much greater than the signal field, we have

$$|\overline{\alpha_{LO}(t)}|^2 \gg |\overline{\alpha_s(t)}|^2. \tag{3.5}$$

The current in the two detectors is proportional to the square of the field amplitude. With a subtraction of the two channels, the current difference becomes

$$I_-(t) \approx 2\alpha_{LO}\left[\Delta X_{1s}(t)\cos\phi + \Delta X_{2s}(t)\sin\phi\right]. \tag{3.6}$$

We thus detect a signal that is proportional to the amplitude of the strong field and depends on the phase difference ϕ. The output signal is then sent to a spectrum analyzer that does a Fourier transform and displays the power spectrum. The power is proportional to the square of current

$$I_-^2 \approx 4\alpha_{LO}^2\left[\Delta X_{1s}^2\cos^2\phi + \Delta X_{2s}^2\sin^2\phi\right] \tag{3.7}$$

By changing the phase difference ϕ we can see either the variance in ΔX_{1s} or ΔX_{2s}.

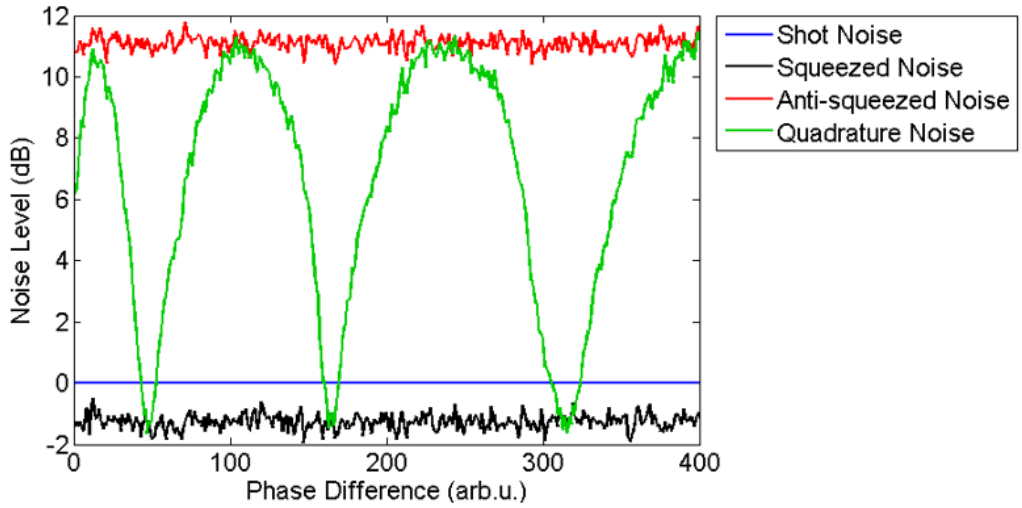

FIG. 3.2: This figure shows a typical data set that we see on the spectrum analyzer. The maximum and minimum noise level are taken when the phase difference between the two fields are fixed to corresponding values. The shot noise level is taken when the signal field is a coherent vacuum, the noise level does not change with respect to ϕ. We use this shot noise as a reference for how much noise suppression, or squeezing we can achieve. The varying quadrature noise trace is taken when we manually change the phase difference ϕ.

From the previous chapter, we know that for a squeezed state, one of the quadrature fluctuations can be smaller than the standard quantum limit (SQL). In Fig. 3.2 we show a typical display of the spectrum analyzer taken at pump intensity of 10 mW and the atomic density of $9.3\times10^{11}cm^{-3}$. Here we see a noise suppression of -1.8 dB of minimum noise below the SQL (noted as the shot noise in the figure) and 11 dB of maximum noise. They are each called squeezed noise and anti-squeezed noise.

3.2 Experimental apparatus

The experimental setup for squeezing generation is described in Fig. 3.3. An external cavity diode laser (ECDL) is tuned by approximately 100 MHz to the red of the $5^2S_{1/2}, F = 2 \rightarrow 5^2P_{1/2}, F' = 2$ transition of ^{87}Rb ($\lambda \simeq 795$ nm). The detuning of the laser can

be slightly changed (within a few hundred MHz) in practice. This is our optimal laser detuning position, but we also have detected squeezing on other transitions of the D1 line of ^{87}Rb atom, we will show these results later in this chapter. The laser output is spatially filtered by passing the beam through a single-mode-polarization-maintaining (SMPM) fiber, linearly polarized using a Glan-laser polarizer (GP) and focused into a 7.5 cm long cylindrical Pyrex cell with isotropically enriched ^{87}Rb vapor and no buffer gas. Unless otherwise specified, we use this cell for all the detections. In our experiments other cells, that have different length, buffer gas or atoms, are also used. The waist of the focused beam (diameter 100 μm at $1/e^2$ intensity level) was located 6.5 cm from the front of the cell, which is an optimized position for squeezing.

The cell was mounted inside a three layer μ-metal magnetic shield to eliminate the magnetic field from the Earth. We can change the temperature of the cell in a range of 21°C to 120°C, corresponding to an atomic vapor density range of 1.4×10^{10} cm^{-3} to 2.0×10^{13} cm^{-3} (see Fig. 3.4).

The interaction of a strong laser field with the ^{87}Rb vapor modifies the vacuum fluctuations in the orthogonal polarization. In order to measure quadrature noise, we rotate the polarization of the strong field and the squeezed vacuum field by 45° and mixed them on a polarization beam splitter (PBS) before sending them to a balanced photodiode (BPD). We thus realize a homodyne detection in which the strong laser field served as the local oscillator (LO) [18, 20]. The relative phase of the two fields is adjusted by tilting the phase-retarding (PhR) plate (a birefringent quarter-wave plate with a crystal axis set parallel to

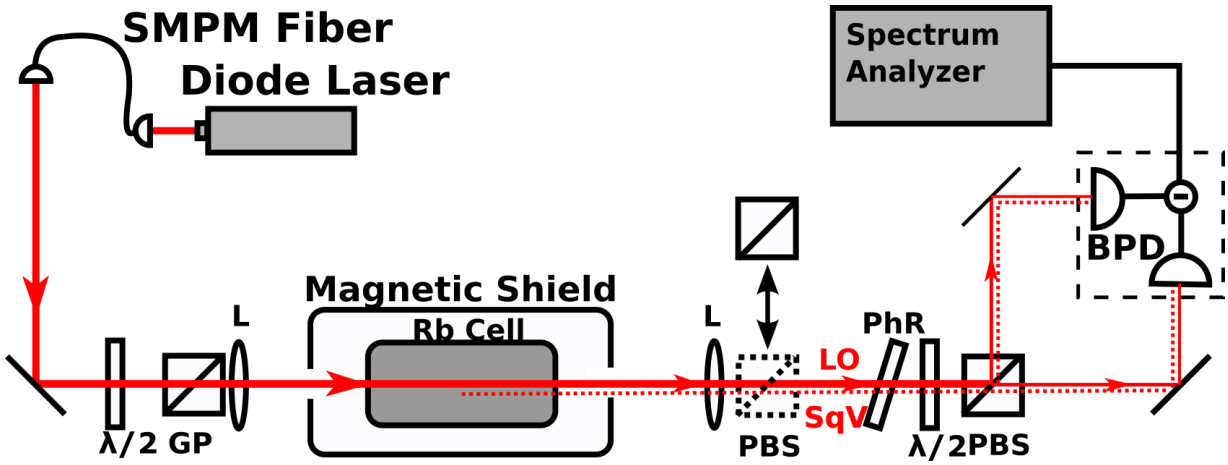

FIG. 3.3: Experimental setup. SMPM is a single-mode polarization-maintaining fiber, $\lambda/2$ is half-wave plate, GP is Glan-laser polarizer, PBS is a polarizing beam splitter, PhR is a phase-retarding wave plate, and BPD is a balanced photodetector.

the LO polarization). All the measurements reported below are performed either at 1 MHz or 800kHz detection frequency with 100 kHz resolution and 30 Hz video bandwidths. To calibrate the SQL level, we insert an additional PBS into the beam after the cell, which rejects the squeezed field and replaces it with a coherent vacuum field. The fluctuations in the coherent vacuum are the quantum noise limit, which we refer to as the shot noise.

At optimal conditions in this setup, we detected noise suppression of 2.0 ± 0.2 dB below the SQL level in the maximally squeezed quadrature and 11 dB of anti-squeezing in the orthogonal quadrature, which is quite typical for these kinds of atomic squeezers.

In this configuration, the squeezed vacuum field and the local oscillator stays in the same path, until the PBS separates the two fields into two different channels of the homodyne detection scheme. The advantage of such arrangement is that the spatial overlap of the strong field and the weak field always stays at a high level. To alter the phase difference between the two fields, we need to place a phase retarder in the light path, usually a wave

plate as is shown in Fig. 3.3.

3.3 Parameters that affect squeezing

In our experiments, there are several parameters that change the squeezing amount we achieve. Without taking into account the spatial properties of the beam, we need to consider the intensity of the beam, the atomic density in the Rb vapor cell, the position of the beam focus in the cell, the length of cell, the buffer gas pressure, the magnetic field, etc.

3.3.1 Choice of cell

The cell that contains the Rubidium atoms has a lot of different configurations, such as the glass cell coating, the buffer gas pressure and the length of cell. In our measurements we used two kinds of cells:

1. ^{87}Rb in vacuum cell, 7.5 cm long.
2. ^{87}Rb in vacuum cell, 1 cm long.

3.3.2 Atomic density vs. temperature

Previous studies of squeezing generated in ^{87}Rb suggested a strong dependence on the density of atomic vapor. The alkali exists in three phases in the cell. The vapor density is determined by the temperature. Steck [42] has summarized equations simulating the

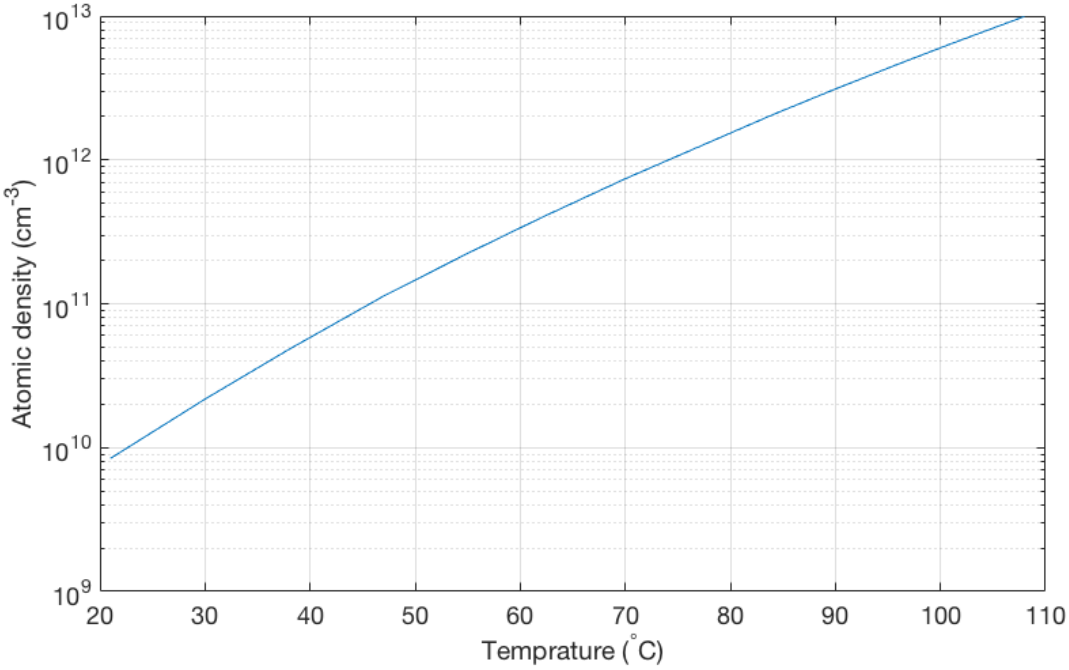

FIG. 3.4: This figure shows the saturated vapor density of ^{87}Rb calculated in Eq. 3.8.

saturated vapor pressure of ^{87}Rb in [42].

$$\begin{aligned} \log_{10} P_V &= -94.05 - \frac{1961}{T} - 0.03772T + 42.58 log_{10} T \ \ (solid\ phase) \\ \log_{10} P_V &= 15.88 - \frac{4530}{T} + 0.0005866T - 2.991 log_{10} T \ \ (liquid\ phase)\,. \end{aligned} \tag{3.8}$$

With ideal gas equation $PV = nRT$, we can estimate the vapor density from the pressure of vapor shown in Fig.3.4.

3.3.3 Beam intensity dependence

The strength of the non-linear interactions between the light field and the atoms largely depends on the beam intensity. When the beam intensity is not strong enough, the

interaction would be too weak to generate any sizeable cross phase modulation. However, high beam intensities saturate the atomic absorption in the cell. In such conditions, the squeezing can be degraded by the saturation of atoms and beam distortion. There is always an optimal beam intensity for squeezing generation.

3.3.4 Beam focus size and position

Intuitively one can imagine that the intensity of beam in the cell, as well as the interaction length would both affect the squeezing result. These factors are affected by the way that we focus the beam in the cell and the spatial mode of the beam. Similarly, we can carry out the optimization of beam focus position and beam spot size by varying the converging lens strength and the cell position. The pump beam mode can be controlled by spatial masks.

3.3.5 Laser detuning

There have been studies that observe noise suppression for varying laser detunings from the hyperfine atomic levels of Rb [43]. In our experiments, we use a diode laser detuned at the $F = 2 \rightarrow F' = 2$ transition of ^{87}Rb D1 line. For comparison, we observe all four transitions for ^{87}Rb atom. In reality, the $F = 2 \rightarrow F' = 1$ transition also exhibits some amount of squeezing for certain choice of cell.

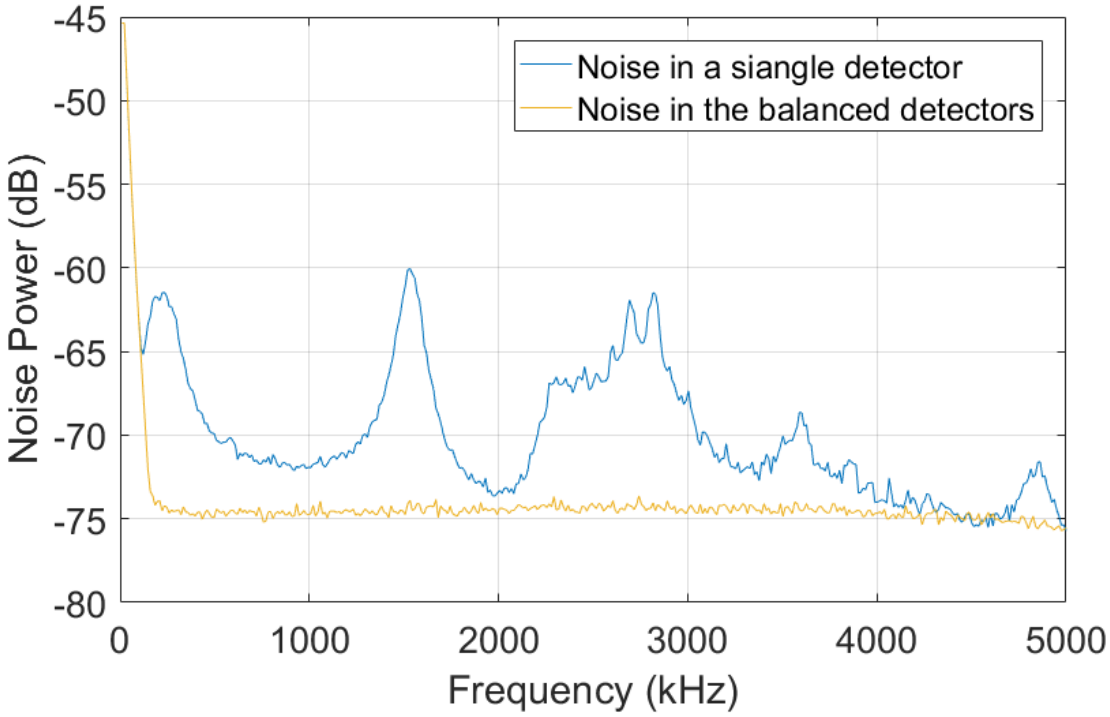

FIG. 3.5: The noise spectrum detected in a single photodetector (blue trace) has many noise peaks. The noise spectrum detected by a pair of balanced photodetectors (yellow trace) is relatively flat.

3.3.6 Detecting frequency

Although our experimental apparatus can generate a broad-band squeezed vacuum field, we want to focus on a particular detection frequency to optimize our squeezing level because there are a few noise peaks in this noise spectrum, and some of them are close to our optimal squeezing frequency (shown in Fig. 3.5). These noise peaks are intrinsic noise in the laser that we can not get rid of. To minimize the influence of these peaks on our detection, in most of our measurements we focus on either 1 MHz or 800 kHz of detection frequency. Previous studies [44, 17] have performed a detailed measurement on the detection frequency comparison to find an optimal frequency of squeezing detection.

CHAPTER 4

Self-Focusing Effect and Its Influence on Squeezing

4.1 Self-focusing effect

Self-defocusing/self-focusing is a well-known nonlinear effect [45, 46]. When an electromagnetic field propagates through a dense medium, the non-linear response of the refractive index change to the intensity of the beam works like a lens, causing a change in the size and the divergence of the output field.

We have discussed in the previous chapter that the optimal condition for squeezing generation involves the intensity of beam. One can imagine that if the beam is experiencing the self-focusing or defocusing effect in the medium, the noise suppression is correspondingly affected. In this chapter we study the beam size change due to the self-focusing

effect in both a Gaussian beam and a beam in a LG_{10} mode. We also study the change of squeezing produced in the cell with the beam size change. This chapter is reproduced from [47].

4.2 Gaussian and vortex beam

Referring back to Chapter 2, we have discussed the Laguerre Gaussian mode of the electromagnetic field. Beams in higher LG modes appear broader than a Gaussian mode and it is easier to observe the beam shape change visually. We can produce an LG beam of $l = 1, p = 0$ (noted as the vortex beam in the following discussion) with a phase mask in our experiment, as is shown in Fig. 4.1. This phase mask consists of eight segments of different optical lengths. When we go around the center of this phase mask, we can expect a phase change of 2π. Such phase modulation can also be achieved with a more sophisticated system such as a liquid-crystal-based spatial light modulator (SLM), which we will talk about later in this dissertation. However, for this chapter we just use the eight-segment optical component to generate the vortex beam.

Our experimental arrangement allowed us to investigate the effect of self-defocusing of the optical fields in Rb vapor at higher atomic density. We place a CCD camera in the beam path after its interaction with the atoms. This camera is a Dragonfly DR2 camera from FLIR. It has 480×640 pixels, the spacing between neighbouring pixels is 7.4 μm. In practice we use a Matlab program to control the camera parameters, such as the shutter time, number of averages and the gain, etc. We capture images of the beam and fit the

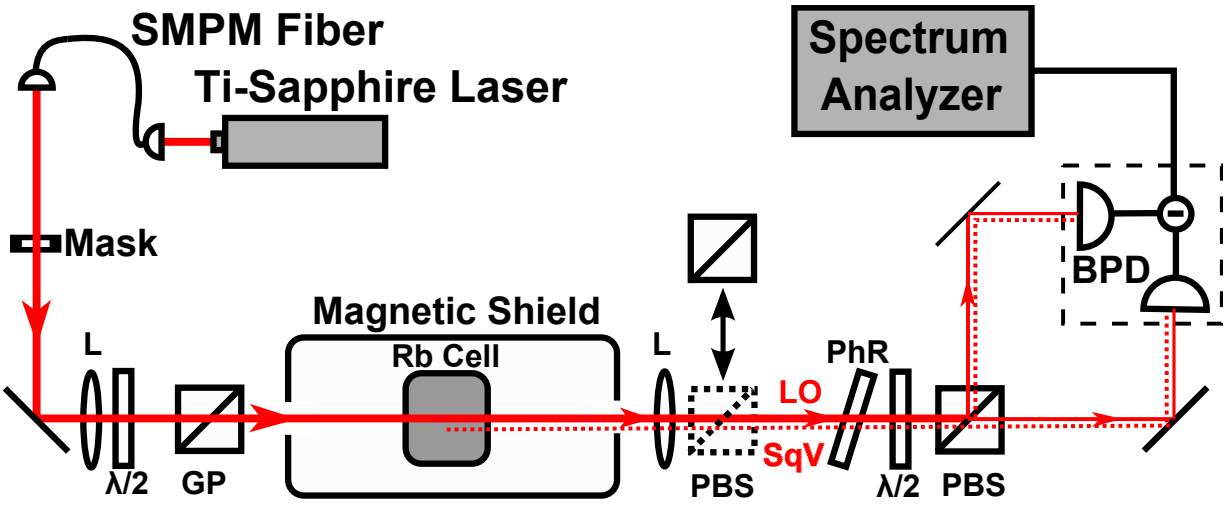

FIG. 4.1: Experimental setup. The mask can change a Gaussian profile beam into a vortex beam.

beam intensity to either the Gaussian distribution,

$$I(r) = I_0 e^{\frac{-2r^2}{w^2}} \tag{4.1}$$

or a vortex beam,

$$I(r) = I_0 \frac{r^2}{w^2} e^{-\frac{2r^2}{w^2}} \tag{4.2}$$

The beam waist w is the parameter we observe to compare the output beam sizes.

Fig. 4.2 shows that we observed a strong defocusing effect for both Gaussian and vortex pump beams, which was more obvious as we increased the density of Rb atoms. Previous work showed (both experimentally and theoretically) that such beam distortion can limit the generation of squeezed vacuum in the four-wave-mixing process [48].

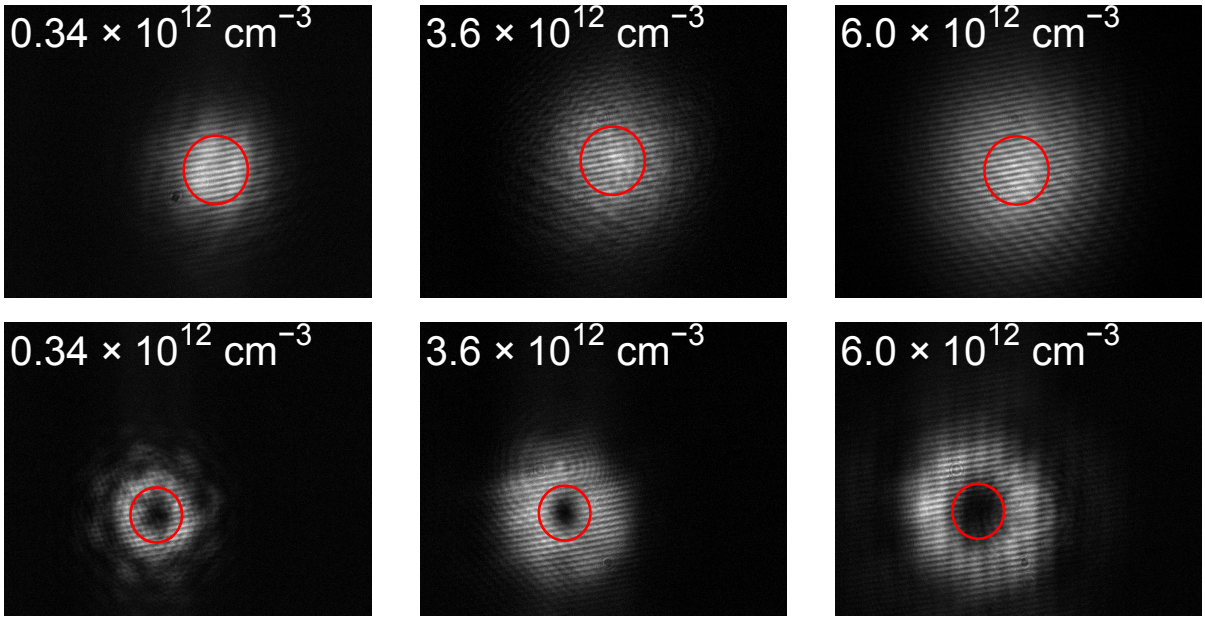

FIG. 4.2: The transverse profiles of a Gaussian (top) and vortex (bottom) beams after interaction with the Rb vapor cell at different atomic densities. The red circles are shown to aid visual comparison of beam sizes in low and high atomic density cases for the Gaussian and vortex beams, correspondingly.

4.3 Correlation of self-focusing and squeezing

Here we present observations of the dependence of squeezing upon the beam intensity and atomic density. In the meantime, we also record the beam size to see how much the beam has been distorted by the self-focusing effect. We carry out these measurement with both a Gaussian beam and a vortex beam. For each measurement we optimized the laser frequency for the highest value of squeezing, within approximately 200 MHz of the $5^2S_{1/2}, F = 2 \rightarrow 5^2P_{1/2}, F' = 2$ ^{87}Rb atomic resonance.

Here, we are using a 1 cm long vacuum cell that has isotopically pure ^{87}Rb inside. We use a Ti-Sapphire laser for stronger pump intensity. For a regular pump beam with a Gaussian distribution in intensity [Fig. 4.3(a)], the best squeezing of 1.8 ± 0.2 dB was

observed at a pump power of 10.5 mW and an atomic density of 2.7×10^{12} cm^{-3}. The measured squeezing level was somewhat worse than previously observed values at this Rb optical transition [20]; possibly due to higher cell temperature (to compensate for shorter cell length).

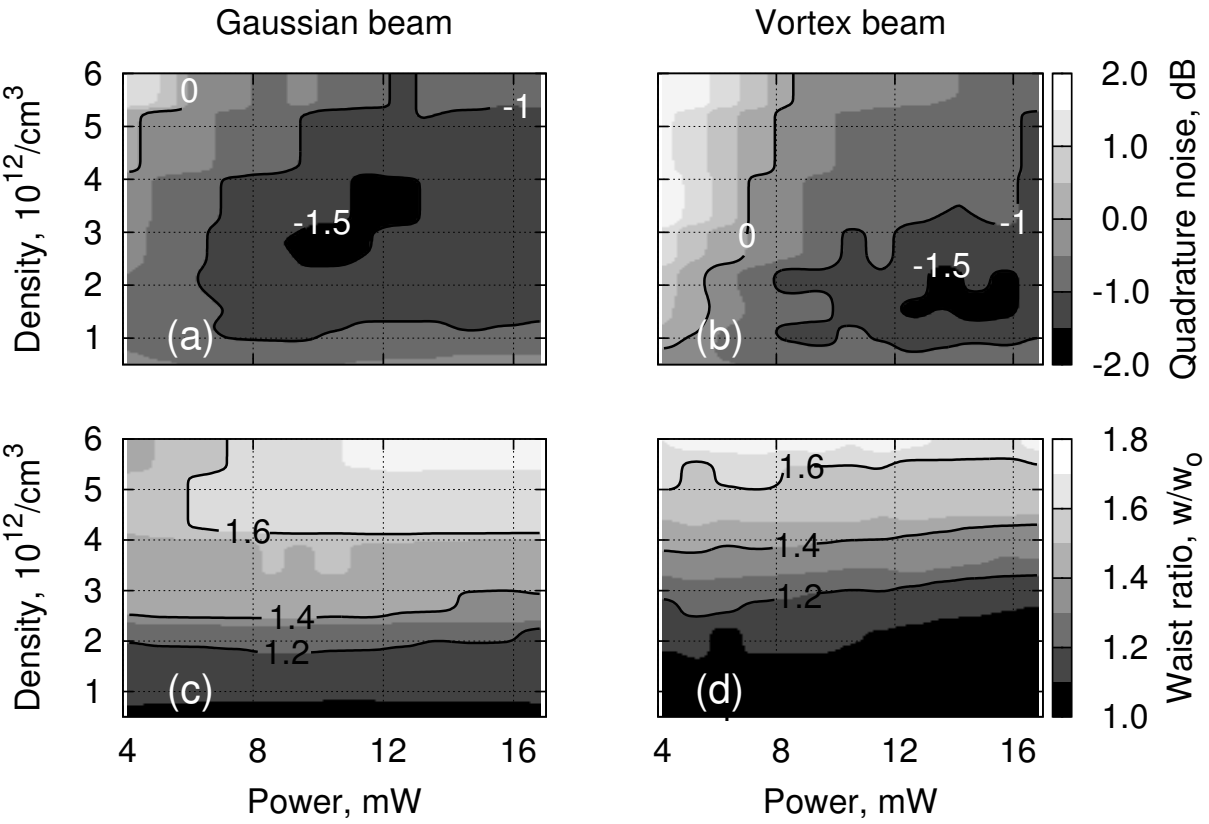

FIG. 4.3: Measured minimum quadrature noise power (top row) and the relative beam expansion (bottom row) for the pump beam with the Gaussian (left column) and Laguerre-Gaussian (right column) distributions as functions of the pump power and the atomic density. The beam expansion is measured as the ratio of the measured waist (w) [from fits (Eq. 4.1) and (Eq. 4.2)] to its value at low temperature (w_0), where self-defocusing was negligible. For quantum noise measurements, zero corresponds to the shot noise level. Spectrum analyzer detection frequency is 1 MHz.

Similar to the previous observation, the maximum squeezing occurred in a small area of the pump power/atomic density parameter space. The optimized value of measured

squeezing with vortex pump beam matched the value obtained using a regular pump beam within the experimental uncertainty. At the same time, the optimal experimental conditions differed in these two cases. For the vortex pump beam, the best squeezing of 1.7 ± 0.2 dB occurred at a higher optical pump power of 14.7 mW and a lower atomic density of $(1.8 \pm 0.3) \times 10^{12}$ cm^{-3}.(Under identical conditions, the squeezing obtained with a Gaussian pump beam was only 1.1 ± 0.2 dB.)

To search for correlations between the beam size variation and observed squeezing level, we recorded the images of the output pump beam intensity distributions for different values of laser power and atomic density matching the experimental parameters of the squeezing level measurements depicted in Fig. 4.3(a,b). Since the intensity distributions of all beams were well-fitted by either Eq.(4.2) (with phase mask inserted) or Eq.(4.1)(with no phase mask), the measurements of the waist parameter w were sufficient to accurately describe beam modifications at various experimental parameters. The results of these measurements are shown in Fig. 4.3(c,d) for both Gaussian and Laguerre-Gaussian pump beams.

In our detection scheme, we used the output pump field as a local oscillator, substantially reducing the sensitivity to the beam distortions (compared to an independent LO beam in Ref. [48]) as long as both the squeezed vacuum and the pump field were spatially overlapped. A simple comparison of the data in Figs. 4.3(a) and (c) reveals that the observed maximum squeezing occurred at the region of moderate (≈ 50 %) beam expansion for the Gaussian beam. The same is true for the vortex pump beam [Figs. 4.3(b)

and (d)]. For a fixed atomic density there is very little variation in the beam diameter with respect to the laser power. Simultaneously, the measured values of squeezing showed much stronger intensity dependence, with squeezing reaching a local maximum at some intermediate power, and then decreasing at higher powers. These observations somewhat contradict the detailed theoretical calculations [49] that the value of squeezing must continuously grow with laser power.

At the same time, this contradiction cannot be explained by the self-defocusing effect either, since the size of the laser beam does not change at the higher intensities compared to the optimal intensity at fixed atomic density. Thus, based solely on these measurements we cannot completely rule out the self-focusing effect, since both beam expansion and squeezing deterioration become more pronounced at high atomic densities. It is possible that as atomic density increases, the spatial modes for squeezed vacuum and the pump field may experience different defocusing, resulting in the reduction in the measured squeezing due to the mode-mismatch at the detection stage. To unambiguously distinguish such differential self-defocusing effect from other nonlinear interactions, such as spontaneous Raman generation and four-wave mixing [50, 51], we need to conduct the experiment using a spatially configurable local oscillator and thus directly map the output spatial mode of the squeezed vacuum.

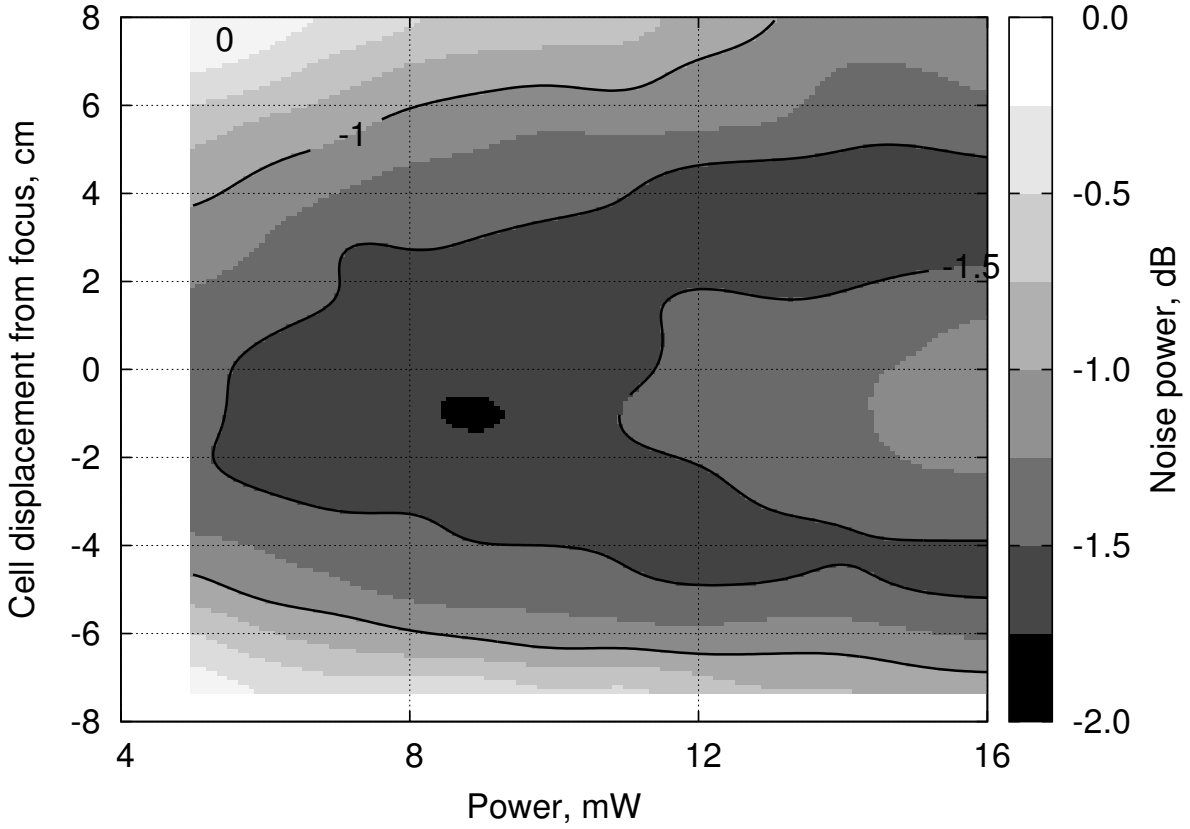

FIG. 4.4: Measured minimum quadrature noise power as a function of position of the focal point and the pump power. Zero displacement corresponds to the Gaussian pump laser focused at the center of the vapor cell. For quantum noise measurements zero corresponds to the shot noise level. Spectrum analyzer detection frequency was 1 MHz.

4.4 Beam focus position

The changes in optimal experimental parameters for different pump beams are not surprising, since the details of the pump beam propagation inside the atomic ensemble are known to have a strong effect on the output squeezed vacuum. For example, Fig. 4.4 shows the variations in the measured squeezing as the magnetic shield, containing the vapor cell, is shifted back and forth along the focused Gaussian pump beam path. Considering the depth of focus of approximately 4.8 cm, we can see that the best value of

squeezing is obtained with the lowest pump power when the cell is positioned around the focal point. Any displacement of the cell away from the focus in either direction results in achieving similar value of squeezing at higher value of the pump power. Since the peak intensity of the first-order Laguerre-Gaussian beam is less than half of the peak intensity of a regular Gaussian beam with the same waist parameter, we expect to see a higher laser power to produce optimal squeezing for the vortex pump beam.

4.5 Summary

We study the dependence of beam waist change on the experimental parameters such as the intensity of beam and the atomic density. We use a pump beam with two kinds of spatial profile, a Gaussian beam and a vortex beam, to monitor the beam size change. These two kinds of pump beam exhibit slightly different amount of squeezing with different optimal conditions. The beam size clearly depends on the atomic density in the cell; as the density goes up, the beam gets expanded. However,in contrast to other theoretical and experimental studies of 4WM process[48], we do not see a direct correlation between self-focusing and noise suppression. Hence self-focusing may not be an important cause of degradation of squeezing.

CHAPTER 5

Multi-Mode Structure of the Squeezed Vacuum Field

All previous experimental and theoretical analysis of PSR squeezing assumed an identical single spatial mode for both the strong pump and vacuum fields, with either fundamental Gaussian [18, 20] or Laguerre-Gaussian [47] transverse profiles.

In this chapter we investigate an interferometric scheme and explain why we start to study the spatial structure of the squeezed vacuum field. We use different masks to modify the beam profile and observe the squeezing level change to study the spatial structure of the beam. To simulate the data, we develop a theory that decomposes the beam structure into a superposition of several high-order Laguerre-Gaussian modes. This chapter is reproduced from [52].

5.1 Assumption in homodyne detection

In Chapter 3, when we talk about the Homodyne detection scheme, there is an intrinsic assumption in the theory. We have assumed that the LO and the squeezed vacuum field have same spatial distribution. However, if the two fields are not perfectly overlapped and the amplitude and phase distributions of them have spatial dependence.

$$\alpha_s(t) = [\alpha_s + \Delta X_{1s}(t) + i\Delta X_{2s}(t)]\, u_s(x,y)\, e^{i\theta(x,y)} \tag{5.1}$$

$$\alpha_{LO}(t) = [\alpha_{LO} + \Delta X_{1LO}(t) + i\Delta X_{2LO}(t)]\, u_{LO}(x,y)\, e^{i\phi} e^{i\vartheta(x,y)} \tag{5.2}$$

$u_s(x,y)$ and $u_{LO}(x,y)$ are the amplitude distributions of the squeezed vacuum and the LO fields. $e^{i\theta(x,y)}$ and $e^{i\vartheta(x,y)}$ are the phase distributions. Taking into consideration such spatial distributions, the signal sent into the spectrum analyzer would be

$$\begin{aligned} I_-^2 \approx\ & \alpha_{LO}^2 \Delta X_{1s}^2 \left[\iint |u_{LO}u_s^* + u_{LO}^* u_s| \cos(\phi + \theta - \vartheta)\, dxdy\right]^2 \\ & + \alpha_{LO}^2 \Delta X_{2s}^2 \left[\iint |u_{LO}u_s^* + u_{LO}^* u_s| \sin(\phi + \theta - \vartheta)\, dxdy\right]^2 \\ & + \left(1 - \frac{1}{2}\iint |u_{LO}u_s^* + u_{LO}^* u_s|^2 dxdy\right) \alpha_{LO}^2 \Delta X_{1,2v}^2 \end{aligned} \tag{5.3}$$

In this case, the spatial distribution of the phase results in a complicated term in the noise. The noise is no longer a simple function of the general phase difference ϕ. The third term of this noise comes from the coherent vacuum field, as is described in a beam splitter model. Both these terms cause a decrease of detected squeezing. The spatial mismatch

between the squeezed vacuum field and the LO might be the reason that the experimental results of noise suppression have not reached the theoretical prediction. To study the spatial distribution of both these fields, we place different kinds of spatial masks in the light path as is described in this chapter.

5.2 Spatial mask and the influence on squeezing

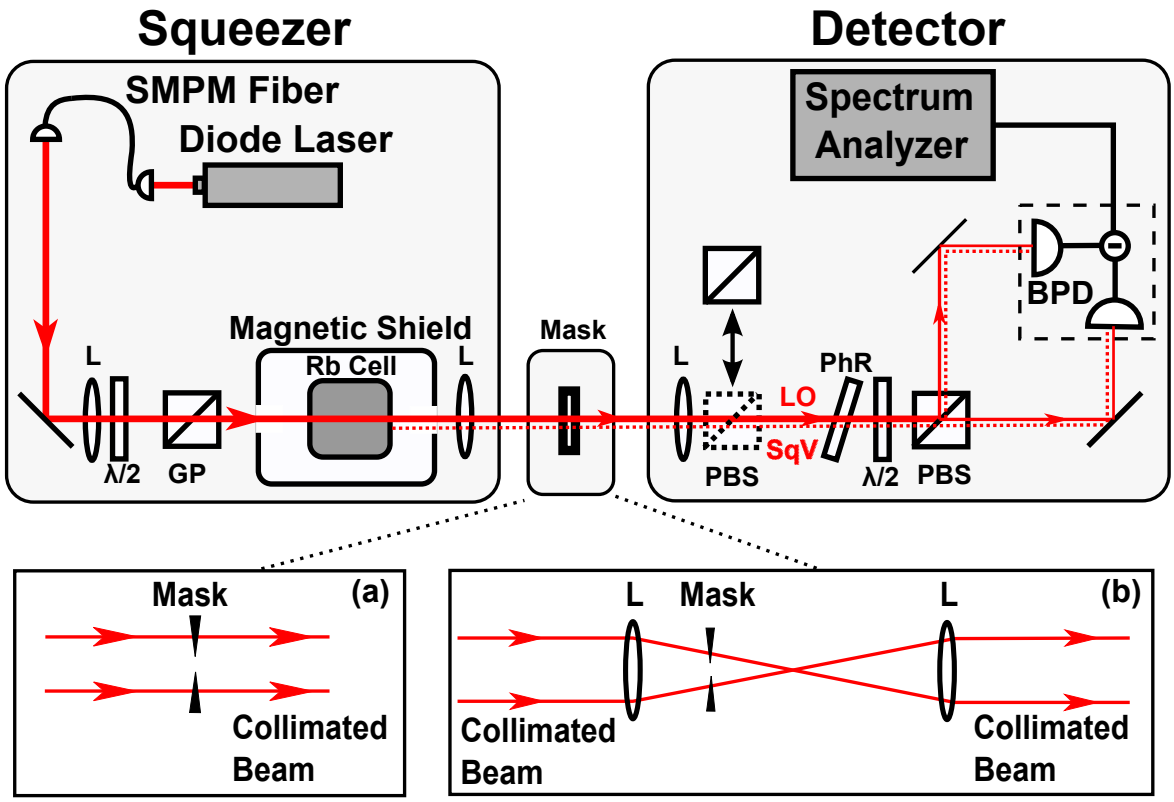

FIG. 5.1: Spatial mask applied to the beam after squeezer. (a) The mask is applied directly to the beam. (b) A pair of lenses is installed and works like a telescope. The spatial mask is applied around the focus.

In our setup we manipulate the squeezed beam from the Rb cell with spatial masks in two regions: in the collimated region (Fig. 5.1(a)) or in the focusing region (Fig.5.1(b)).

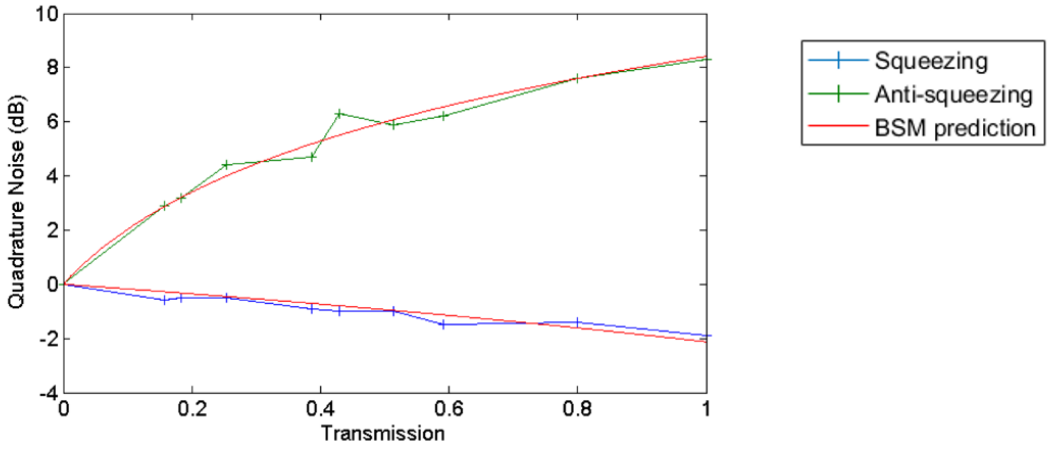

FIG. 5.2: This figure shows the squeezing amount we can see with the beam after cell being attenuated by the neutral filters. The green and blue dots are each the measured values of anti-squeezed and squeezed noise level, with different strength of attenuation. The solid red line is the theoretical calculation for continuous change of transmission.

All the beam masks are cylindrically symmetric. Based on a single-mode description of the optical field, one would expect the changes in the detected quantum noise in all cases to depend only on the total optical transmission T, and to be accurately described by the beam-splitter expression:

$$SqV_{\mathrm{out}} = 10 \cdot \log_{10}[\mathrm{T} \cdot 10^{\mathrm{SqV_{in}}/10} + (1 - \mathrm{T})], \tag{5.4}$$

where $SqV_{\mathrm{in,out}}$ are the quadrature noise measured in dB before and after the mask. To validate such theory we make simple measurements with setup in Fig. 5.1 (b), with the mask to be neutral density filters that can decrease the intensity uniformly.

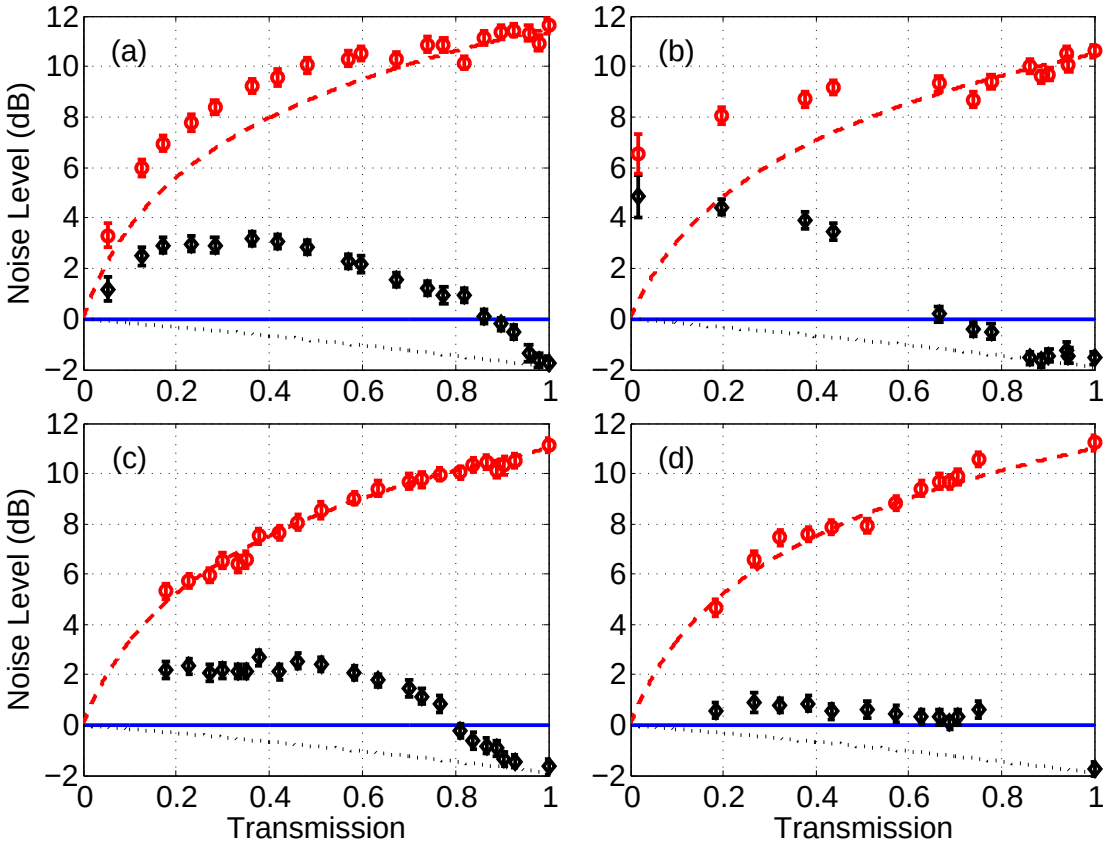

FIG. 5.3: Measured minimum (diamonds) and maximum (circles) quadrature noise when the laser beam is partially blocked by (a) an iris mask, (b) a disk mask, (c,d) the combined masks, formed by both iris and the disk. For all measurements the horizontal axis indicates the fraction of LO intensity, transmitted through the mask. In (c) the central disk alone blocked 8% of the LO power and in (d) the power loss was 25%. Dashed and dotted lines indicate the prediction of the single-mode model, described by Eq. (5.4). The zero of the vertical axis corresponds to the shot-noise noise level.

5.2.1 Spatial mask in the collimated region

We can classify the spatial beam mask as dot masks and iris masks, the former blocking the center of the beam and the latter blocking the outer rim of the beam. Also we apply a combination of these two masks. We use an adjustable iris and a set of fixed sized dots. The position of these masks in space can be fine-tuned with x-y optical mounts. Since the spatial masks change the LO power, we carefully re-calibrate the shot noise for each of

these masks as in Eq. 5.4.

The modifications of the quantum noise by different types of masks are presented in Fig. 5.3. Clearly, the experimentally measured noise values deviate significantly from the naive expected dependencies; shown in Fig. 5.3 as dashed and dotted lines, indicating non-trivial spatial correlations [53, 23]. For example, even small losses of about 10% (for the iris mask) and 30% (for the disk mask) bring the squeezed quadrature noise significantly above shot noise. Moreover, for the disk mask, even at small transmission ($T < 5\%$), the quantum noise in both quadratures is more than 5 dB above shot noise, see Fig. 5.3(b). In contrast, Eq. (5.4) predicts that in all cases we should expect the squeezed noise to approach the SQL monotonically from below, never exceeding the shot noise level.

To gain additional insight about the spatial distribution of the squeezed vacuum field, we look at the noise of a ring-like slice of the laser beam. To do this we constructed a mask consisting of a fixed size opaque disk and a variable size iris. Fig. 5.3(c,d) represents modifications of transmitted quantum noise by such masks where the fixed disk sizes are characterized by 8% and 25% blockage of LO power. Again, Fig. 5.3(c,d) shows that we are not able to improve the measured noise suppression below that of the unobstructed beam, even though the anti-squeezing noise follows the uniform loss model much better. Perhaps, such combined masks are able to block especially noisy spatial modes.

5.2.2 Semi-classical theory of the spatial multi-mode generation

Since the previous theory [14, 54] was performed in the plane-wave approximation, our theoretical collaborator, R. N. Lanning, develop a model that accounts for the possibility of the higher-order spatial modes. Treating the light classically, we start with the inhomogeneous wave equation

$$\nabla^2\mathbf{E} - \frac{1}{c^2}\frac{\partial^2\mathbf{E}}{\partial t^2} = \frac{1}{\epsilon_0 c^2}\frac{\partial^2\mathbf{P}}{\partial t^2}, \tag{5.5}$$

where $\mathbf{P} = \frac{N}{V}\langle\hat{\mathbf{d}}\rangle$ is the polarization induced in the medium, $\langle\hat{\mathbf{d}}\rangle = \sum_{m,n}\mu_{mn}\rho_{mn}$ is the expectation of the dipole operator in an atomic level basis $\{|n\rangle\}$, and μ_{mn} are dipole moment matrix elements. We use the density matrix expression for the polarization, along with the slowly varying envelope and paraxial wave approximations, to transform Eq. (5.5) into a propagation equation in terms of the envelope functions $\tilde{E}$ and $\tilde{\rho}$:

$$(\frac{\partial}{\partial z} - \frac{i}{2k}\nabla_\perp^2)\tilde{E} = \frac{ik}{2\epsilon_0}\frac{N}{V}\sum_{m,n}\mu_{mn}\tilde{\rho}_{mn}. \tag{5.6}$$

Next we apply a simple model in which we treat the D1 line of ^{87}Rb as a double-Λ scheme[55]. We treat the input field as a superposition of two circularly polarized fields characterized by Rabi frequencies Ω_+ and Ω_-, corresponding to right- and left-circular polarizations. We solve for the density matrix elements, and since our pump field is in fact linearly polarized, we convert to the linear polarization basis and distinguish the

propagation equations for the two envelope functions in terms of the Rabi frequencies:

$$\hat{L}\,\Omega_{x,y} = -2\kappa\Omega_{x,y}\frac{|\Omega_{x,y}|^2}{|\Omega|^4}(\gamma_0 + 2i\frac{|\Omega_{x,y}|^2}{\Delta}) \tag{5.7}$$

where $\hat{L} \equiv (\frac{\partial}{\partial z} - \frac{i}{2k}\nabla_\perp^2)$, k is the wave number, κ is the coupling constant, γ_0 is the decay rate, $|\Omega|^4 \equiv (|\Omega_x|^2 + |\Omega_y|^2)^2$, and Δ is the detuning. We further note that Ω_y is the Rabi frequency of the y-polarized pump field and Ω_x is the Rabi frequency of the x-polarized vacuum field. The homogeneous equation solved in cylindrical coordinates yields the LG family of solutions $u_{l,p}(\vec{r})$, given by Eq. (2.12). We obtain the mode structure of the output beam by avoiding a numerical calculation and proceeding with a weak scattering approximation in the following way. We assume $\Omega_{x,y}$ on the right-hand side (r.h.s.) of Eq. (5.7) take the form of the input modes, i.e., $\Omega_{x,y} \to \varepsilon^0_{x,y}u_{0,0}(\vec{r})$, $|\Omega|^4 \to \varepsilon_y^4$, and use the fact that $\varepsilon_x^0 \ll \varepsilon_y^0$ to simplify Eq. (5.7):

$$\begin{aligned}\hat{L}\Omega_{x,y} = -u_{0,0}(\vec{r})\,\big[\kappa\gamma_0\,\frac{\varepsilon^0_{x,y}}{|\varepsilon_y^0|^2}\,u_{0,0}(\vec{r})^* u_{0,0}(\vec{r}) \\ +i\frac{\kappa}{\Delta}\,\varepsilon^0_{x,y}\,(u_{0,0}(\vec{r})^* u_{0,0}(\vec{r}))^2\big].\end{aligned} \tag{5.8}$$

In this approximation we can regard the r.h.s. of Eq. (5.8) as the source of the Rabi frequency on the left-hand side (l.h.s.) of Eq. (5.8), and with this observation we define the appropriate sources ρ_x and ρ_y to simplify the notation, i.e., we transform Eq. (5.7) into $\hat{L}\Omega_{x,y} = \rho_{x,y}(\vec{r})$. We can now use a Green function method [56] to write an integral

expression for $\Omega_{x,y}$:

$$\begin{aligned}\Omega_{x,y} = &\int r'dr'd\phi'\; K(\vec{r}|\vec{r}\,')\Omega_{x,y}^{\text{homo}}(\vec{r}\,') \\ &+ \int dz' \int r'dr'd\phi'\; G(\vec{r}|\vec{r}\,')\rho_{x,y}(\vec{r}\,'),\end{aligned} \tag{5.9}$$

where $\Omega_{x,y}^{\text{homo}}(\vec{r}\,') = \epsilon_{x,y}^{\text{homo}} u_{0,0}(\vec{r})$ represents the portion of the beam passing through the cell unaltered, $K(\vec{r}|\vec{r}\,')$ is the propagator, and $G(\vec{r}|\vec{r}\,')$ is the Green function for Eq. (5.8). An adjustable parameter, related to the absorption and properties of the cell, characterizes the relative strength of $\rho_{x,y}$ to $\Omega_{x,y}^{\text{homo}}$. Thus, once $K(\vec{r}|\vec{r}\,')$ and $G(\vec{r}|\vec{r}\,')$ are known the problem is solved. The most effective way to write the propagator (and consequently the Green function) is in terms of the LG modes. We define the propagator and Green function accordingly:

$$\begin{aligned}K(\vec{r}|\vec{r}\,') &\equiv \sum_l \sum_p \; u_{l,p}^*(\vec{r}\,')\; u_{l,p}(\vec{r}), \\ G(\vec{r}|\vec{r}\,') &\equiv \Theta(z - z')K(\vec{r}\,|\vec{r}\,'),\end{aligned} \tag{5.10}$$

where Θ is the Heaviside step function.

We further utilize the LG modes with an expansion of the sources $\rho_{x,y}$:

$$\begin{aligned}\rho_{x,y}(\vec{r}) &= \sum_l \sum_p c_{l,p}\; u_{l,p}(\vec{r}), \\ c_{l,p}(z) &= \int r dr d\phi\; u_{l,p}^*(\vec{r})\; \rho_{x,y}(\vec{r}).\end{aligned} \tag{5.11}$$

We pause to point out that, since the propagation equation inherits no ϕ dependence from

either the atoms or the input fields, the beam solutions will be limited to $l = 0$ modes. This is clearly seen through the integral for the $c_{l,p}$ coefficients by noting $\rho_{x,y} = \rho_{x,y}(r, z)$ and separating the ϕ phase from the LG mode:

$$c_{l,p}(z) = \int r dr \rho_{x,y}(r, z)\, u^*_{l,p}(r, z) \int_0^{2\pi} d\phi\, e^{il\phi}. \tag{5.12}$$

As one can see, the ϕ integral vanishes for $l \neq 0$. The beauty of this approach is that, as a consequence of the orthogonality of the LG modes, we are able to find an analytic solution which retains the mode structure of the field. Using Eq 5.10,5.11, 5.12 in Eq. 5.9 we arrive at the final solutions for the Rabi frequencies in the weak scattering limit:

$$\Omega_{x,y} = \Omega^{\text{homo}}_{x,y}(\vec{r}) + \sum_p u_{0,p}(\vec{r}) \int_{\text{cell}} dz' c_{0,p}(z'). \tag{5.13}$$

One can perform these integrals with ease and our calculations show that the summation converges rapidly for $p \leq 5$. Now, we proceed by introducing a new experimental investigation which can expose the complicated LG *phase* structure predicted by the preceding theory, and hidden in the beam mode structure.

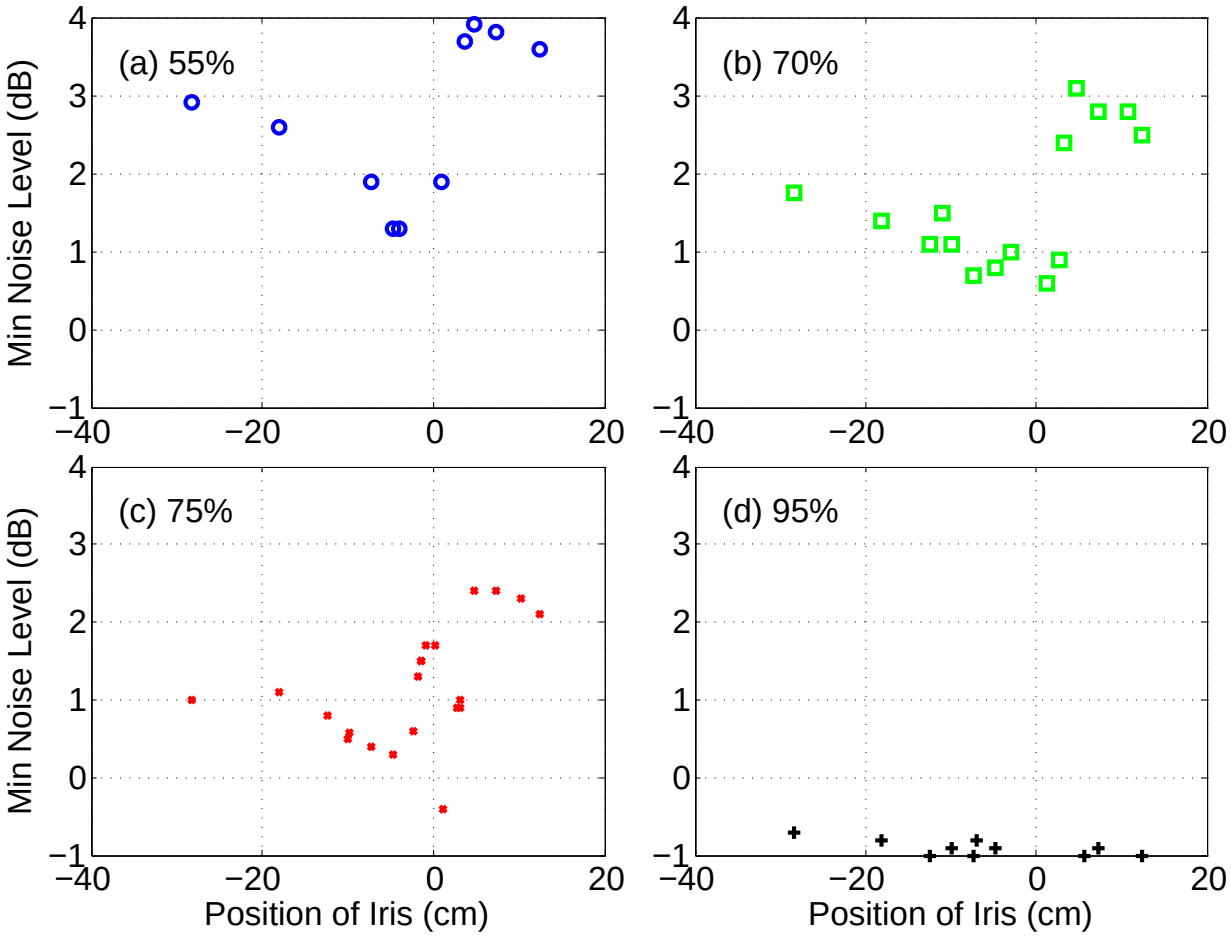

FIG. 5.4: Minimum quadrature noise vs. a variable iris position. The iris size was adjusted to maintain constant transmission of the LO beam for each trace as depicted in the legend: 55% (a, circles), 70% (b, squares), 75% (c, crosses), and 95% (d, plus signs).

5.3 Spatial properties of the focused output beam

5.3.1 Spatial mask in the focusing region

Referring back to the field description of LG mode in Eq. (2.12), we have the Gouy phase $(2p + |l| + 1)\arctan(z/z_R)$. This phase factor has a sharp phase shift around the focus. If our LO and squeezed field do in fact have a mixed LG structure, then we should observe asymmetries about such a focal point; otherwise, the beam will have a simple

Gaussian profile on both sides of the focus. Referring back to Eq. (5.13), we see that the semi-classical theory predicts a mixture of 5 different Gouy phases.

Therefore, we built a one-to-one telescope to create an extra focal point and displaced the iris mask down the telescope to investigate the LG structure. The modified setup is depicted in Fig. 5.1(b). As we move the iris along the beam, we change its size to maintain the same transmission of the LO beam, i.e., we kept the same ratio of the iris radius and the $w(z)$. If our LO and squeezed field do in fact have a mixed LG structure, then we should observe asymmetries about such a focal point; otherwise, the beam will have a simple Gaussian profile on both sides of the focus. Therefore, our data is mostly affected by the different Gouy phase change in different spatial modes. We track the quantum noise in the maximally squeezed quadrature versus position of the iris. As one can see in Fig. 5.4, the quantum noise changes very drastically as the iris is moved right around the focal point. In the case that the iris size is large enough to allow high transmission, we see that the noise level does not change much as the iris is moved along the beam (see Fig. 5.4(d)). On the other hand, as transmission of the mask decreases, the noise in the squeezed quadrature go above shot noise (see Fig. 5.4(a, b, and c)). Perhaps the most surprising is the noise dependence for the 75% transmission mask (see Fig. 5.4(c)), where one can see a very sharp drop of the noise into the global minimum around z=1 cm, where it is squeezed below the shot-noise level. Similar but less pronounced behavior can be observed for the 70% transmissive mask (see Fig. 5.4(b)). Such drop indicates that we may have accidentally found a relatively pure squeezed mode with our spatial mask,

which can be considered as a simple mode sorter. If we apply a better programmed, more sophisticated mask, it is possible to extract only the most squeezed mode and push the squeezed noise even lower.

For the same setup (see Fig. 5.1(b)), we map the transmission and minimum noise curve vs. the position of irises with fixed diameters, as shown in Fig 5.5. The transmission of the LO exhibits some degree of asymmetry. The position of the maximum transmission shifted as we varied the iris size (see Fig. 5.5(a)). For the irises with 93% and 86% peak transmission, there are more than one local minima. We use Eq. (5.13) to predict the transmission level of the two LO fields (see Fig. 5.5(b)) and it is in a qualitatively good agreement with our experimental data (see Fig. 5.5(a)). We would like to again emphasize, that it is the interplay of Gouy phase shifts in the mode superposition (Eq. (5.13)) that create this peculiar dependence on the iris position around the focal point.

Based on the beam splitter model (Eq. (5.4)), we calculate the expected minimum noise as in Fig. 5.5(d). In the theoretical plot, the noise is always lower than shot noise since the model does not take into account the excess noise. But, we can still compare it with Fig. 5.5(c) and find that the overall behavior is quite similar. In both plots, the minimum in the noise power traces shift to the right, i.e., farther from the cell as the iris size shrinks. The qualitative agreement of these plots is further evidence of the LG structure of the squeezed vacuum beam. A more rigorous description necessarily requires a quantum treatment of both the light-matter interaction and the interaction with the spatial masks. Therefore, we next develop a simple second quantized theory that incorporates the LG

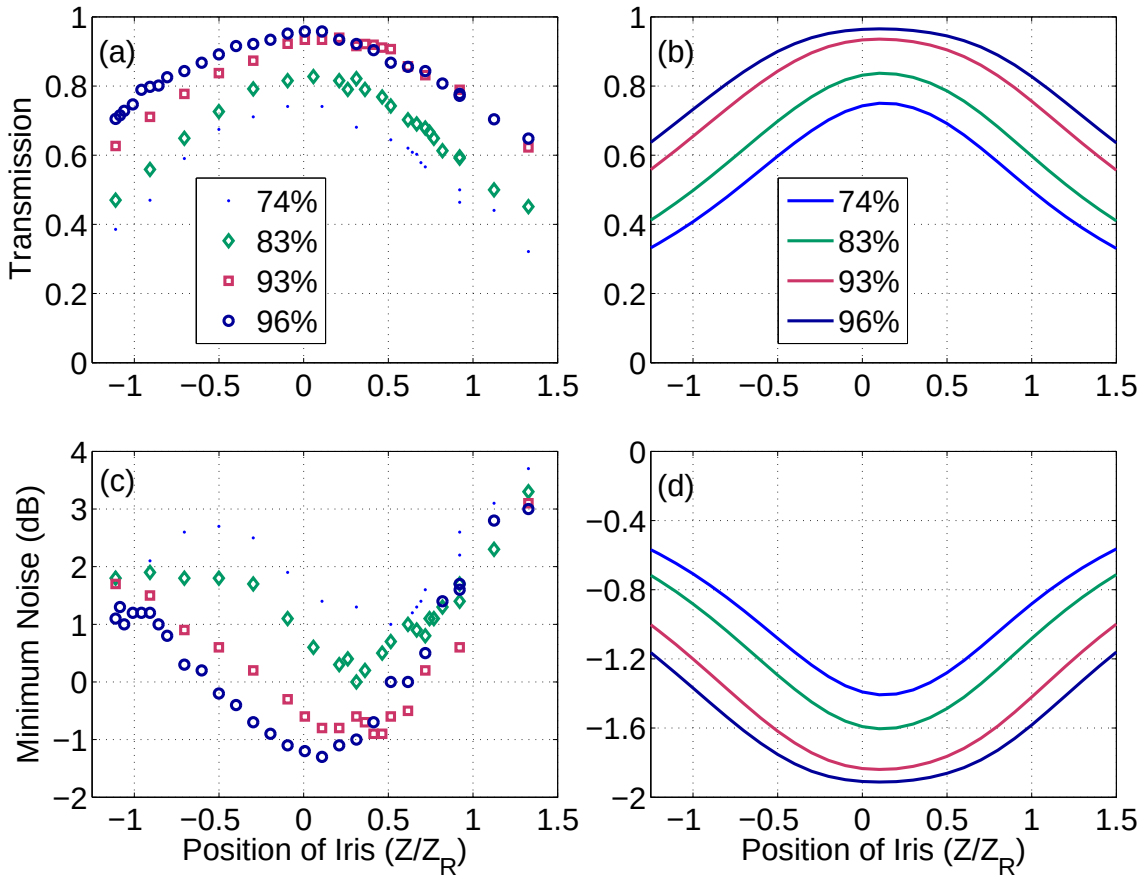

FIG. 5.5: Comparison of the experimental and theoretical (left and right column) dependencies of the LO beam transmission (top row) and the squeezed field minimal noise power (bottom row) on the iris position for several fixed iris sizes. The legend denotes the peak transmission for each iris. The Rayleigh range is Z_R =2.5 cm. To calculate transmission and noise power, we used Eq. (5.13) and Eq. (5.4).

structure of the semi-classical beam and predicts the distribution of the quantum noise for the individual LG modes.

5.3.2 Multi-mode quantum noise calculations

We now extend our previous semi-classical treatment of the multi-mode light-atom interactions to develop a second quantized theory that predicts the underlying modal

structure of experimentally realized squeezing. At first glance, one can think that our homodyne detection scheme is immune to any spatial mode structure modifications since the strong field, used as the local oscillator (LO), also passes through the vapor cell, so any spatial profile distortion are shared by both the squeezed optical field and the local oscillator. However, we still need to take into account the mode structure. Even if the overlap between squeezed modes and the local oscillator modes is perfect, distinct modes are going to contribute into the measured noise level differently. Therefore, to predict the resulting measured quantum noise, one must first predict the squeezing parameters for each of the vacuum mode, and then, using the semi-classical solution for the LO, simulate the results of the homodyne detection.

We proceed with the conventional single mode second quantization procedure, modifying it along the way to incorporate the higher-order LG mode structure. It is commonplace to represent the atomic polarization by a power expansion in the applied electric field strength E [57]:

$$P = \sum_{n=1}^{\infty} P^{(n)} = \epsilon_0(\chi^{(1)}E + \chi^{(2)}E^2 + \chi^{(3)}E^3 + ...). \tag{5.14}$$

Typically, in the plane wave approximation, one would define the n^{th} order susceptibility as $\chi^{(n)} = P^{(n)}/\epsilon_0 E^n$ [58]. However, in the paraxial approximation, special care must be taken since the electric field is confined to the beam axis. We reduce the electric field and polarization to z dependence by integrating over a slice of the vapor cell perpendicular to the light beam. This is necessary, since the electric field dies off rapidly in r, and

valid, since we are well within the validity of the paraxial approximation, i.e., each mode's transverse profile simply rescales with z. Thus, from this point forward we are careful to distinguish the strictly z-dependent electric field and polarization

$$\begin{aligned} P(z) &= \int_{\text{cell}} r dr d\phi P(r,\phi,z) \\ E(z) &= \int_{\text{cell}} r dr d\phi E(r,\phi,z). \end{aligned} \tag{5.15}$$

Now that we have carefully chosen this representation, we may define the n^{th} order susceptibility as

$$\chi^{(n)} \propto \frac{P^{(n)}(z)}{E^n(z)}, \tag{5.16}$$

where $P^{(n)}(z)$ is the n^{th} order polarization in response of the input field $E(z)$. Then we further expand the optical polarization in terms of the LG modes:

$$P^{(3)}(r,\phi,z) = \sum_{l,p} c_{l,p} u_{l,p}, \tag{5.17}$$

where $c_{l,p} = \int r dr d\phi \; u^*_{l,p} \; P^{(3)}(r,\phi,z)$. Motivated by this expansion, we introduce the accompanying LG susceptibility for each LG mode:

$$\chi^{(3)}_{l,p}(z) \equiv \frac{P^{(3)}_{l,p}(z)}{E^3(z)}, \tag{5.18}$$

where we define the LG polarization $P^{(3)}_{l,p}(z) \equiv \int_{\text{cell}} r dr d\phi \; c_{l,p} u_{l,p}$. In this representation, the LG susceptibility not only carries information about the LG spatial structure, it can

be interpreted as the mechanism for "cross-talk" between the Gaussian pump and the vacuum LG modes during the non-linear interaction. Therefore, we define an interaction Hamiltonian density following the prescription of Ref. [59]:

$$\mathcal{H}_{l,p} \propto i\hbar\, \chi^{(3)}_{l,p}(z)\big(\hat{a}^2_{l,p}\hat{b}^{\dagger 2} - \hat{a}^{\dagger 2}_{l,p}\hat{b}^2\big) \tag{5.19}$$

where $\hat{a}_{l,p}$ is the l,p spatial mode operator of the vacuum and $\hat{b}$ is the pump input mode. Thus, the full interaction Hamiltonian is

$$\mathrm{H} \propto \int_{\mathrm{cell}} dz \sum_{l,p} \mathcal{H}_{l,p}. \tag{5.20}$$

We proceed by assuming the y-polarized pump mode is an undepleted coherent state and make the substitutions $\hat{b} \longrightarrow \beta e^{-i\omega_p t}$ and $\hat{b^\dagger} \longrightarrow \beta^* e^{i\omega_p t}$. This leads to the evolution operator

$$\mathrm{U} = \exp\Big[\int_{\mathrm{cell}} dz \sum_{l,p} (\eta^*_{l,p} t\ \hat{a}^2_{l,p} - \eta_{l,p} t\ \hat{a}^{\dagger 2}_{l,p})\Big] \tag{5.21}$$

where $\eta_{l,p} \equiv \chi^{(3)}_{l,p}\beta^2$. Next, making the substitution

$$\xi_{l,p} \equiv 2\int_{\mathrm{cell}} dz\ \eta_{l,p} t \equiv r_{l,p} e^{i\theta_{l,p}} \tag{5.22}$$

we transform Eq. (5.21) into the form of the familiar "squeezing" operator with the addition

of the LG indices [60]:

$$\hat{S}(\xi) \equiv \mathrm{U} = \exp\Big[\sum_{l,p} \frac{1}{2}(\xi^*_{l,p}\ \hat{a}^2_{l,p} - \xi_{l,p}\ \hat{a}^{\dagger 2}_{l,p})\Big]. \tag{5.23}$$

An inspection of Eq. 5.21 reveals that the behavior of the LG modes through the focus in the vapor cell drastically effects the distribution of squeezing among the modes. Likewise, the Gouy phase of each mode and the cell position/dimensions effectively determines the squeezing angle of each mode.

After defining the proper squeezing operator, we can find the variances of the LG quadrature operators:

$$\begin{aligned} \hat{X}_{1\,l,p} &= \frac{1}{2}(\hat{a}_{l,p} + \hat{a}^\dagger_{l,p}) \\ \hat{X}_{2\,l,p} &= \frac{1}{2i}(\hat{a}_{l,p} - \hat{a}^\dagger_{l,p}) \end{aligned}. \tag{5.24}$$

The calculation is not particularly straightforward, but the result [61],

$$\begin{aligned} \big\langle (\Delta \hat{X}_{1,2\,l,p})^2 \big\rangle = \frac{1}{4}\Big[&\cosh^2 r_{l,p} + \sinh^2 r_{l,p} \\ &\mp 2 \sinh r_{l,p} \cosh r_{l,p} \cos\theta_{l,p}\Big] \end{aligned} \tag{5.25}$$

is the familiar textbook result, but written for a particular LG mode [60]. In other words, in this simplified scenario, each mode of squeezing has the statistics of a single squeezed mode. Furthermore, the photocurrent (difference) variance is a weighted sum of quadrature variances (some squeezed, some anti-squeezed) of all modes which overlap the LO [62]. As

we have shown previously, only the modes with $l = 0$ are relevant to our experiment due to symmetry and consideration of angular momentum. Then one can show

$$\begin{aligned}\left\langle (\Delta i_d)^2 \right\rangle \propto \sum_p |O_p|^2 [e^{-2r_p} \cos^2(\text{Arg } O_p) \\ + e^{2r_p} \sin^2(\text{Arg } O_p)],\end{aligned} \tag{5.26}$$

where we define the overlap integral O_p as

$$O_p \equiv \frac{\int \Omega_{\text{LO}}^* \phi_p \, d^3r}{\sqrt{\int |\Omega_{\text{LO}}|^2 \, d^3r}}, \tag{5.27}$$

Ω_{LO} is the local oscillator, and ϕ_p is the spatial function of the p^{th} mode (in this case simply the $u_{0,p}$ LG mode). To visualize these results we use the squeezed vacuum Wigner function; labeled here for each l, p mode,

$$\begin{aligned}W_{l,p}(x,y) = \frac{2}{\pi} \exp\Big[-(y^2 + x^2) \cosh r_{l,p} \\ + \big((x^2 - y^2) \cos\theta_{l,p} + 2xy \sin\theta_{l,p}\big) \sinh r_{l,p} \Big].\end{aligned} \tag{5.28}$$

5.3.3 Second quantization deployed

Using quantum state tomography, we have reconstructed the Wigner function for our squeezed vacuum state (Fig. (5.6a)). This Wigner function corresponds to noise suppression of 1.9 ± 0.2 dB below the SQL level in the maximally squeezed quadrature (the best suppression we were able to achieve in our experimental geometry), a modest amount of

squeezing compare to the predictions of the single-mode theory [14, 54, 63]. However, the preceding theory suggests that more significant squeezing could be hiding in the spatial mode structure of the beam. To facilitate the comparison with the experimental results, we employ the second quantized theory to determine the value of the coupling constant κ in Eq. 5.7 so that the minimum quadrature noise of the theoretically calculated output measured via homodyne detection provides 1.9 dB noise suppression in the X_1 quadrature, i.e., $\theta/2 = 0$. The Wigner function of such a hypothetical state is plotted in Fig. (5.6b). The same simple second quantized theory also gives us the decomposition of this state into various LG modes: first, we follow the preceding progression using the polarization derived in the semi-classical section (r.h.s. of Eq. (5.7)) and the solution Ω_y (Eq. (5.13)) for the y-polarized beam since it is used as the LO during detection. Then, we re-scale the coupling constant such that the weighted sum of quadrature variances (Eq. (5.26)) reproduces the same squeezing of our hypothetical state. To take care of the scaling, we first recognize that since $\theta = 0$, Eq. (5.25) reduces to $\left\langle (\Delta \hat{X}_{1,2\,l,p})^2 \right\rangle = (1/4)e^{\mp 2r_p}$. Furthermore, in the limit of a strong LO, the photo-current difference variance is

$$\left\langle (\Delta i_d)^2 \right\rangle \propto 4|\mathcal{E}_{\mathrm{LO}}|^2 \left\langle (\Delta \hat{X}(\theta))^2 \right\rangle \tag{5.29}$$

where $\hat{X}(\theta) = (1/2)(\hat{a}e^{-i\theta} + \hat{a}^\dagger e^{i\theta})$ is the field quadrature operator at the angle θ. Therefore, combining Eq. (5.26) and Eq. (5.29) for the special case $\theta = 0$, we impose that the scaling

parameter γ satisfy the equation

$$|\mathcal{E}_{\rm LO}|^2 e^{-2r_{\rm exp}} = \sum_p |O_p|^2 [e^{-2\,\gamma\, r_p} \cos^2(\text{Arg } O_p) + e^{2\,\gamma\, r_p} \sin^2(\text{Arg } O_p)] \tag{5.30}$$

where $r_{exp} \approx 0.565$ is the experimental squeeze parameter and $|\mathcal{E}_{\rm LO}|^2 = \int r dr d\phi\, \Omega^*_{\rm LO}\Omega_{\rm LO}$. We solve for γ and determine the re-scaled LG squeeze parameters $r'_p = \gamma\ r_p$ and point out that the squeeze angles $\theta_p = \text{Arg}(\xi_p)$ remain the same.

TABLE 5.1: Squeezing Parameters for Various Modes

p	r'_p	$\theta_p/2$	$\lvert O_p\rvert$	Arg(O_p)
0	1.297	160°	0.995	71°
1	0.315	113°	0.091	101°
2	0.149	97°	0.031	123°
3	0.029	25°	0.006	76°
4	0.011	171°	0.004	38°
5	0.010	18°	0.002	160°

Figure (5.7) shows the Wigner functions for the squeezed LG modes, which comprise the hypothetical state, the $p = 3$ and higher modes are omitted since they show no appreciable squeezing. Table 5.1 summarizes the squeezing parameters and overlap integrals for different modes. It is important to point out that if only the fundamental mode $p = 0$ could be isolated, its minimum quadrature noise would have been measured to be more that 11 dB below the shot noise. The $p = 1$ by itself (if isolated) would have displayed -3 dB of squeezing, but at a different quadrature angle. Higher-order modes have less effect on the combined mode, as is seen in Table 5.1. Thus, we find that there is actually much more squeezing available in the individual modes, but in combination the measurable

noise suppression is much worse due to the fact that the squeezing angles are out of phase. This deterioration is independent on the atomic excess noise [54, 63], that is not taken into account in our simple theoretical model and that can further reduce the measured squeezing value. We hypothesize that the different Gouy phase for each mode rotates the squeezing angle for that mode at a different rate.

5.4 Summary

We demonstrate that the PSR squeezer may generate a multi-spatial-mode squeezed field. We develop a semi-classical model, which qualitatively describes our experimental observation. Additionally, we present a simple second quantization procedure that shows how quadrature noise can be varied between LG spatial modes. Our results have application to improved single-mode squeezing and the production of squeezed light in higher-order modes upon demand.

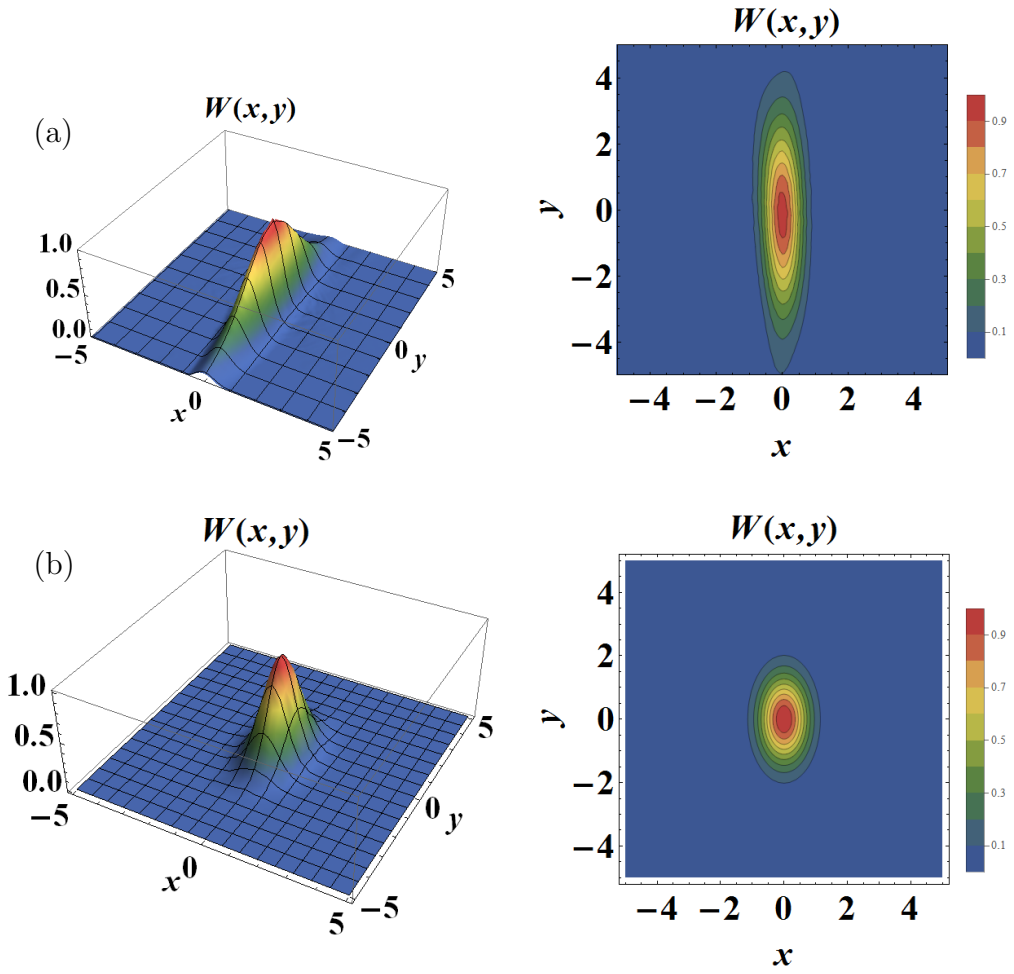

FIG. 5.6: Wigner function of (a) the experimentally realized squeezed state and (b) a hypothetical minimum uncertainty state with 1.9 dB of squeezing along the X_1 quadrature, shown here in 3D and contour. The simple second quantized theory predicts the multi-mode structure (Fig. (5.7)) that results in the same level of measured squeezing via homodyne detection. The axis labels x and y are proportional to the X_1 and X_2 quadratures respectively. The Wigner function has been rescaled by the peak amplitude of the vacuum Wigner function.

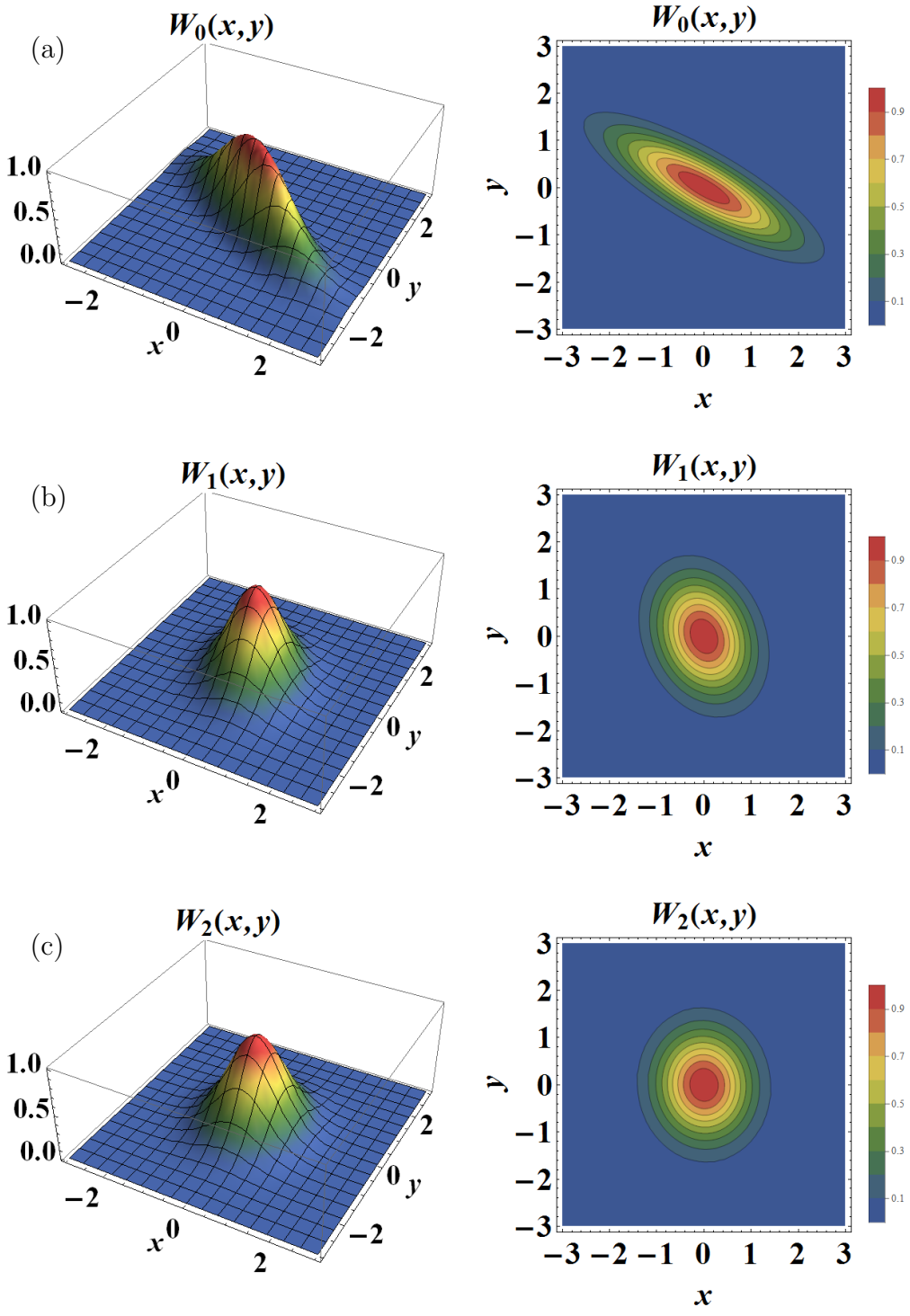

FIG. 5.7: The Wigner functions for the $p = 0 - 2$ modes ((a),(b),(c) respectively) which, when measured simultaneously via homodyne detection, recreate the example Wigner function depicted in (Fig. (5.6). The $p = 3$ and greater modes are omitted since they appear essentially as vacuum modes. The axis labels x and y are proportional to the X_1 and X_2 quadratures respectively. The Wigner functions have been rescaled by the peak amplitude of the vacuum Wigner function.

CHAPTER 6

Multi-Pass Setup and Optimization

In thermal atomic ensembles, it is expected that the strength of the interaction and, thus, the overall performance, increases at higher optical depth [64, 65, 33, 14, 49]. In practice, however, once an optimal value of an optical depth is reached, further optical depth increase leads to deterioration of the desired outcome and/or increasing optical noise. Such behavior of PSR squeezing has been observed by several experiments [16, 47], and yet failed to be reproduced by the simple PSR squeezing theory, even if it included some known negative density-dependent effects (e.g., spin-exchange collisions, radiation trapping, etc). Recently, we have demonstrated that worse-than-expected experimentally observed PRS squeezing can be caused by the modification of spatial mode decomposition of both squeezed vacuum and pump fields as a result of interaction with atoms [52]. Similar multimode generation has also been reported in the non-degenerate four-wave mixing processes [66, 67, 68, 23, 24].

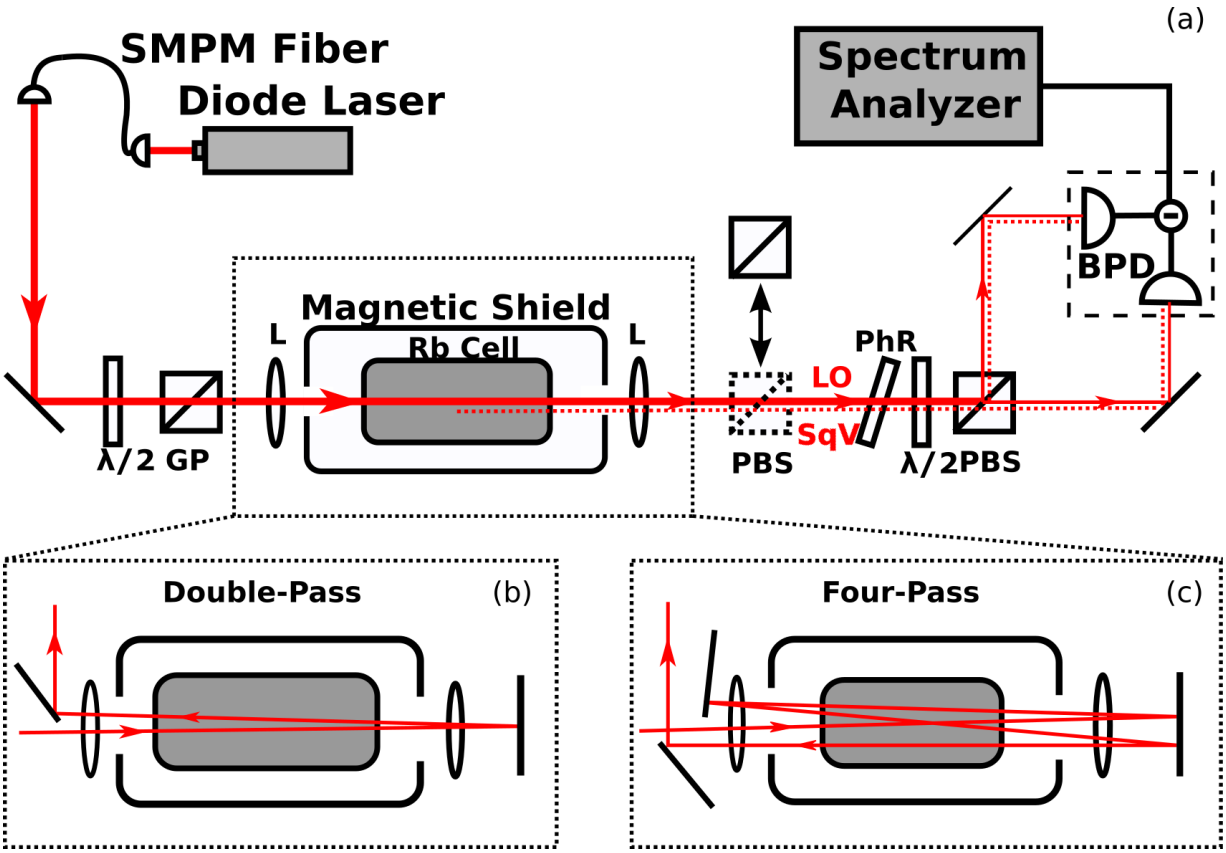

FIG. 6.1: (a) Experimental setup. SMPM is a single-mode polarization-maintaining fiber, $\lambda/2$ is half-wave plate, GP is Glan-laser polarizer, PBS is a polarizing beam splitter, PhR is a phase-retarding wave plate, and BPD is a balanced photodetector. (b) and (c) show the geometry for double and quadruple pass correspondingly.

In this chapter we investigate the behavior of PSR squeezing as a function of optical depth, varying independently both of its components: density of atoms and the interaction length. Specifically we compare the maximum amount of squeezing achievable when the laser beam travels through a vapor cell once or several times. We also let the light pass through two independent identical Rb vapor cells. In both cases, we observe higher amount of squeezing for the case of light traversing the cell twice at lower temperature, even though the overall value of optical depth in both cases were comparable. A possible explanation for our results may originate from non-trivial atomic density scaling of higher-

order spatial modes generation. Our theoretical calculations suggest that fewer higher-order spatial modes are excited when the pump beam travels through a longer cell length at lower temperature than when it interacts with a shorter atomic ensemble at higher atomic density. That matches our experimental observations.

6.1 Single pass vs. multiple pass configuration comparison

The multi-pass experimental setup for is shown in Fig 6.1. The cell we use in this experiment is a 7.5 cm-long vacuum cell. The detection frequency of the spectrum analyzer is 800 kHz. We place mirrors before and after the cell to propagate the beam through the medium for several passes. We carry out a comparison of squeezing levels in three cases, namely directing the pump beam through the vapor cell once (single pass), two times (double pass) or four times (quadruple pass). We map the squeezing level as a function

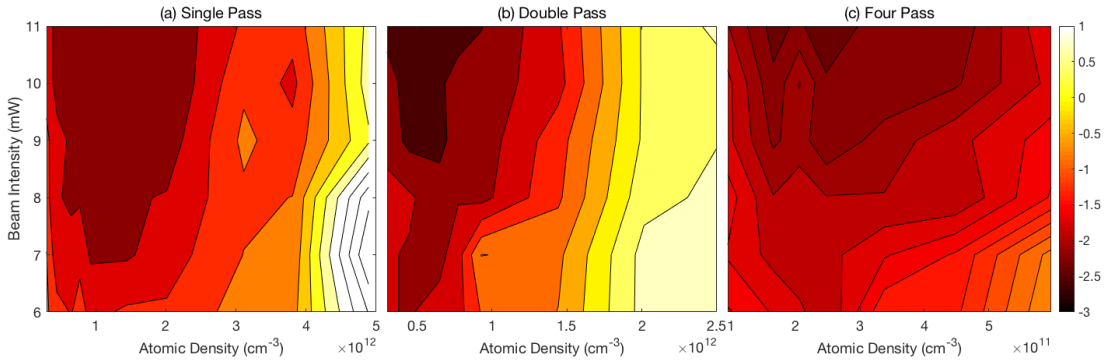

FIG. 6.2: Map of squeezing level vs. beam intensity and atomic density for single, double and quadruple pass. The darkest areas in the plots represent the highest level of quantum noise squeezing.

of the pump beam intensity and atomic density, as shown in Fig. 6.2. On all occasions, a higher beam intensity is always preferred, and the best squeezing was observed at the maximum available laser power of 11 mW.

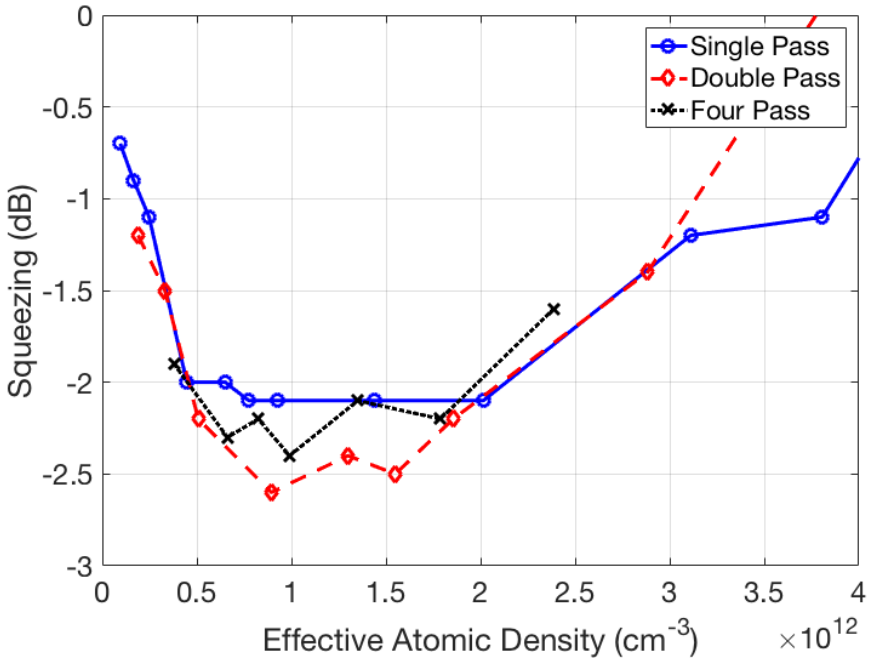

FIG. 6.3: Squeezing dependence on the effective atomic density in the three multi-pass setups. Effective atomic density is defined as the real atomic density times the number of passes.

In the case of a single pass, the best value of squeezing measured is -2.0 dB at an atomic density of 9.3×10^{11} cm^{-3}. When the optical pass number is doubled, a squeezing level of -2.6 dB is achieved at the atomic density 4.3×10^{11} cm^{-3}, showing a substantial improvement over the single pass case. When the optical pass number is doubled again (quadruple pass), we saw a decrease in the measured squeezing amount (-2.2 dB at 2.4×10^{11} cm^{-3}). However, in this configuration, maintaining good collimation of the beam became challenging due to space restrictions, so that the output beam emerged noticeably expanded, which may have lead to the lower observed squeezing.

In Fig. 6.3, we take a slice of these plots at 11 mW of beam intensity. The squeezing amount as a function of effective atomic density, defined as the atomic number density times the total number of passes that the beam travels through the medium. The trends of the three cases agree very well: at first, the measured squeezing increases with optical depth, reaching its maximum, and then starts to deteriorate. Interestingly, in each configuration the best squeezing occurred at approximately the same effective optical depth, even though the best achievable values are different.

This difference can be explained if we analyze the dependence of high-order spatial mode generation during the light-atom interaction. As we demonstrated previously in Chapter 5, the presence of these high-order modes can deteriorate the measured value of squeezing by two factors. First, the difference in the mode decomposition between the pump field (that serves as a local oscillator for our detection scheme) and the vacuum field reduces the effectiveness of homodyne detection. Second, the difference in quantum noise modifications for different spatial modes result in a mismatch between the detection quadrature providing best value of squeezing for different modes, and overall reduction of detectable squeezing when the mixture of spatial modes reaches the detector.

The example of high-order mode generation in the pump field is shown in Fig. 6.4. As expected, for lower atomic density the intensity distribution of the pump beam is well approximated by the the fundamental Gaussian mode $p = 0$. However, at the limit of high atomic density the output intensity exhibits a more complicated structure, showing some ring formation, characteristic of the higher-order Laguerre-Gauss modes. This behavior

is even clearer in the mode decomposition diagrams, shown in Fig. 6.4. It is clear that even though the fundamental Gaussian mode dominates, the contribution of the first $p = 1$ mode increases dramatically with temperature. This pump beam modes analysis is carried out by M. Guidry.

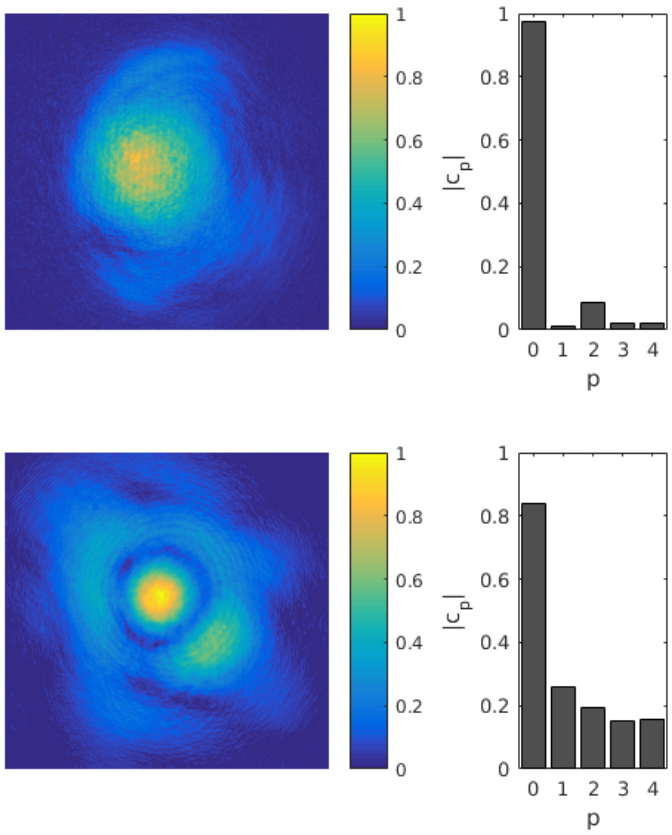

FIG. 6.4: Intensity distribution of the pump field after the cell at *(top)* low temperature ($T = 26°$C, $N = 10^{10}$cm^{-3}) and *(bottom)* high temperature (($T = 111°$C, $N = 1.2\times10^{13}$cm^{-3}), and the calculated deconvolution of the Laguerre-Gaussian modes $L_p^{\ell=0}$.

Identification of the exact mode decomposition of the vacuum field is a more complicated task, and at the moment, we do not have a reliable method for achieving this, although it is under development. However, we can theoretically calculate it using the

method developed in Ref.[69]. Fig. 6.5 shows the difference in the amplitudes of the generated high-order modes c_p for $p = 1$ to $p = 5$ in the case where the number density of atoms is doubled and when the interaction length is doubled. It is easy to see that increasing the length results in significantly less efficient higher order mode generation, even though formally the optical depth in both cases was the same. This asymmetry, however, should not be too surprising. The underlying interaction is nonlinear and strongly intensity-dependent, which means that in our case of a tightly focused pump beam the different sections of the beam along its propagation affect the spatial beam profile differently, in a rather complex way. This effect might be the reason we do not see improvement of squeezing when we increase number of passes from two to four. The theory above is developed by our theoretical collaborator R. N. Lanning.

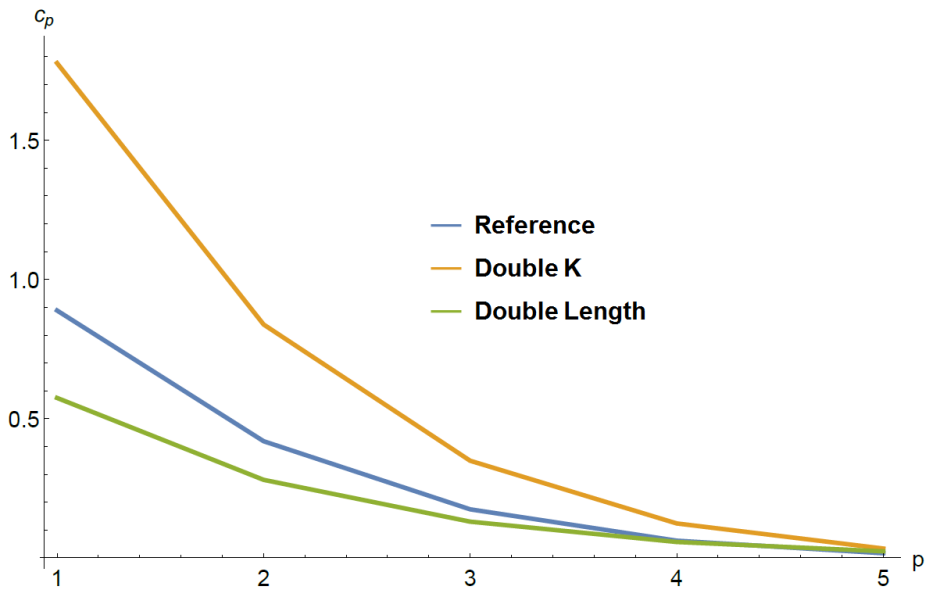

FIG. 6.5: The calculated relative amplitudes of the higher order Laguerre-Gausse modes $L_p^{\ell=0}$ for a case of doubling the density of the atomic ensemble and of doubling the propagation length.

6.2 Two-cell configuration

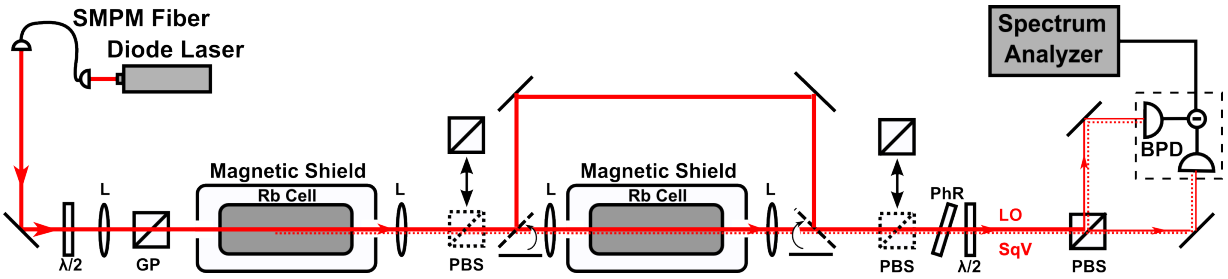

FIG. 6.6: A modified experimental setup with two independent vapor cells. All the abbreviations are the same as in Fig. 3.3

.

To further investigate the effect of multiple interaction of pump and squeezed vacuum optical fields with atoms, we use a modified experimental setup, shown in Fig. 6.6. Namely, we add another identical Rb vapor cell in the setup to make an "unfolded" double pass setup. Before starting the measurements we verify that the single-pass squeezing measurements lead to the identical results in either cell, and the atomic density calibration in the two cells are carefully performed. Such configuration allows us to avoid some of the limitations of the previous setup, namely the inability to independently control various parameter of the experiment, such as the relative position of the beam focus and the cell. The usage of two different vapor cells allows us to independently vary their temperatures and positions. In addition, it is possible to insert the polarizing beam splitter after the first cell effectively removing any quantum noise modifications but preserving any changes in the intensity distribution of the pump field resulting from the interaction with atoms in the first Rb cell. Thus, for all the experiments we perform two sets of measurements: one with the pump and the vacuum fields propagating through both cells without modi-

fications (which is roughly equivalent to the "folded" double pass measurements), and a filter-first-cell case, in which any squeezed field generated in the first cell is rejected, so the measured squeezing reflects only the pump field modified by the first cell.

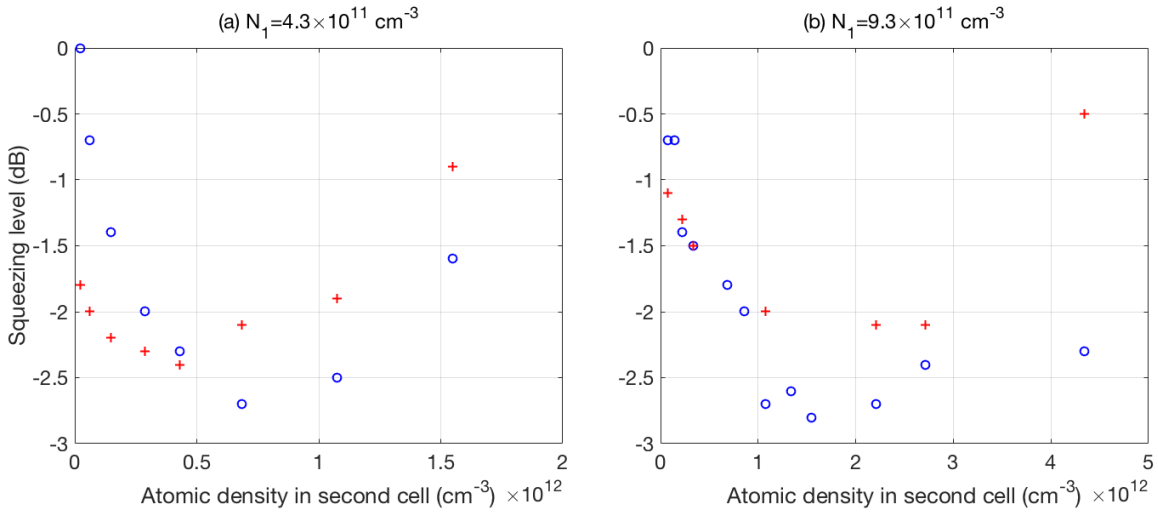

FIG. 6.7: A measurement of squeezing dependence on second cell density in the two-cell system. N_1 is the atomic density in the first cell. In (a) the atomic density of the first cell is 4.3×10^{11} cm^{-3} and in (b) it is 9.3×10^{11} cm^{-3}. Crosses represent the squeezing amount in total and circles correspond to the case when a PBS is inserted after the first cell so that the first-cell-generated squeezing is filtered.

It is possible to change the atomic density of each cell independently, and we also study the effect of changing the atomic density in the second cell. We fix the atom density in the first cell, first at 4.3×10^{11} cm^{-3} - the optimal condition for the double-pass squeezing generation, then at 9.3×10^{11} cm^{-3}, which results in the highest value of the measured squeezing in the single-pass configuration. We vary the atomic density in the second cell, giving squeezing levels shown in Fig. 6.7. The best squeezing (-2.8 dB) is obtained at $N_1 = 9.3 \times 10^{11}$ cm^{-3} and $N_2 = 1.6 \times 10^{12}$ cm^{-3}. It is easy to see that in all cases there exists again an optimal atomic density at which the measured squeezing is optimized. If the squeezed vacuum propagates through both cells (crosses), we unsurprisingly observe the

best squeezing when both cells are at the same atomic density, 4.3×10^{11} cm^{-3}, replicating the optimal conditions observed for the double-pass experiment, shown in Fig. 6.2(b). If the first cell is tuned to the optimal single-pass condition, the best squeezing is measured at somewhat higher values of second cell's atomic density, although there is no further improvements compared to the output of the single cell.

We also observe that if the squeezed vacuum field generated in the first cell is filtered by the polarizing beam splitter, we are able to measure the amount of squeezing after the second cell (-2.8 dB) exceeding both single-cell or double-cell best squeezing. This observation implies that the pump modifications due to the interaction with the first cell result in more favorable conditions for generation of squeezed vacuum in the second cell. Thus, it may be possible to further improve squeezing by actively optimizing the spatial mode decomposition of the pump field. These experiments are currently under investigation.

Our experimental results also display strong dependence of the observed amount of squeezing on the relative position of the cells and the focal points of the optical beams. Such behavior agrees with our previous observations that the exact decomposition of the high-order spatial modes is sensitive to the geometry of the interaction, and changes depending on where in the cell the pump beam is focused. We change the relative position of the beam focus and the cell center for each of the two cells. The relative position of the cell is defined in a way such that we assume the positions of the two beam focii are not changing with atomic density or cell positions. 0 position is when the center of the cell is located

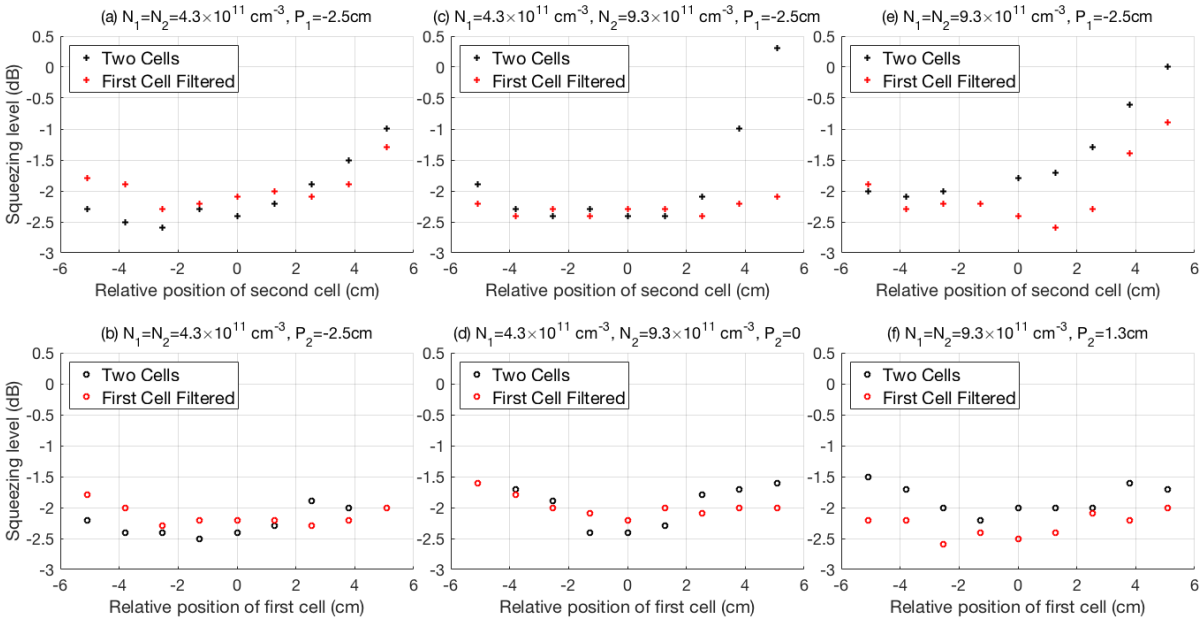

FIG. 6.8: The dependence of squeezing amount on position of first (circles) and second cell (crosses). Black represent the squeezing is measured when both cells are present. Red (light grey) is when an addition PBS is placed after the first cell and filters the squeezed field generated in the first cell.

at the beam focus position, and positive means that the cell center is after focus, i.e. the beam focus lies in the front part of cell. As is shown in Fig. 6.8(a), (c) and (e), we first put the front cell at its optimal position, where we have best single-cell-squeezing, and optimize the position of the latter cell in three different atomic density combinations. We see that when both cells have atomic density of 4.3×10^{11} cm^{-3}, the best squeezing occurs at second cell position $P_2 = -2.5$ cm (Fig. 6.8(a)). But when we only increase the atomic density in first cell to 9.3×10^{11} cm^{-3}, the best squeezing occurs at $P_2 = 0$ (Fig. 6.8(c)), and when both cells have atomic density of 9.3×10^{11} cm^{-3}, the best squeezing occurs at $P_2 = 1.3$ cm (Fig. 6.8(e)). Next, we go through the optimization for the front cell position as is plotted in Fig. 6.8 (b), (d) and (f), with the second cell located at the optimal position we found each in Fig. 6.8(a), (c) and (e). This measurement of best squeezing and optimal

position partly explains why we did not see improved squeezing when we increase pass number from two to four in the previous experiment.

6.3 Summary

We investigate the behavior of PSR squeezing in case of single or multiple interaction of light with atoms. More specifically, we compare the achievable amount of squeezing after the pump beam traveled through the vapor cell once, or the light after the cell was retroreflected, and the squeezing was measured after the second pass through the cell. As expected from the general principle of nonlinear interactions, the amount of observed squeezing strongly depends on the optical depth of the atomic medium. However, we find that even though the optimal squeezing is observed at the same value of the optical depth for the single and double pass configurations, the overall value of squeezing is better for the double-pass configuration, when the cell was maintained at the lower temperature. Quadruple pass configuration also yields to the optimal squeezing at approximately same value of the optical depth, although less squeezing is observed compare to the double pass, probably due to lack of proper beam shape control in this complicated geometry. Moreover, we also study the squeezing in the case of two independent cells, and also observed strong sensitivity of the observed improvement of measured squeezing in case of double interaction at lower atomic density. These observations are consistent with our recent finding that the deterioration of squeezed vacuum with optical depth can be (at least partially) explained by the increasing contributions of high-order spatial modes. Since the process of their

generation seems to be less effective in case of extended length of the optical medium compare to the atomic density increase, a possible avenue toward further improvement of squeezing is squeezing generation in a low-finesse cavity, in which the pump field interacts with atoms multiple times, at lower density of atoms. Our current results also add an interesting twist to a long discussion on the equivalence of achieving the high optical depth by increasing the number of atoms or by extending the length of the interaction medium. We show that in the case of spatially multimode nonlinear interactions these two methods may lead to different results, and thus one of them can be preferrable for a particular application.

In addition, our measurements indicate that it may be possible to further improve squeezing by tailoring the pump spatial profile before the interaction. This conclusion is based on our observation of improved squeezing obtained using the pump field after its interaction with atoms once, as compare to the ideal Gaussian spatial profile. We are currently investigating this possibility.

CHAPTER 7

Modification of the Spatial Structure of the Beam

As is demonstrated in Chapter 5, the squeezed vacuum is generated in a multi-mode structure and has non-perfect mode match with the LO. Under such circumstances, the detected squeezing amount is lower than expected. To compensate for the bad mode match, we need to know the real mode structure of the squeezed vacuum. But it is impossible to observe the spatial structure of the squeezed field directly with a normal CCD camera since the beam is too weak as a vacuum field. Hypothetically, we could use mode sorters to change the mode structure by design and analyze the resulting squeezing as we did in Chapter 5. However, the spatial masks we applied were too rough to serve as an effective mode sorter.

In this chapter, we present the work on programming the mode structure with a spatial

light modulator to optimize squeezing in this chapter. Also, we utilized a quantum-noise-limited camera which can detect a few photons to observe both the LO and the squeezed vacuum. By analyzing the spatial noise distribution from the beam photon counts, we can see the spatial structure of the beams.

7.1 Liquid crystal based spatial light modulator

We placed a liquid crystal based spatial light modulator (SLM) in the beam light path to change the beam phase profile. The SLM we use is a Meadowlark X-Y Spatial Light Modulator. The SLM is consisted of 512 $\times$ 512 pixels with pixel size of 15 μm. Each pixel is a piece of liquid crystal, it has an alignment angle with respect to the screen. The angles of these liquid crystals have a response to the voltage that is applied to them and generate phase retardation to the light that hits the pixel. With a pre-programmed voltage distribution applied on the SLM pixels and a known voltage-phase translation function, we can control the phase modulation to the beam.

With one SLM, phase modulation and amplitude modulation can be applied to the beam simultaneously [70]. Theoretically we can use any combination and achieve all possible shapes of a beam [71, 72]. In our experiment, for simplicity, we applied only phase modulation to the beam to get better squeezing. It is worth mentioning that such beam reshaping actually does not generate ideal mode we implant [73].

7.1.1 Reshape of beam

In the experiment with an SLM in the beam, we carried out two sets of squeezing optimizations with the SLM placed at different positions. We can either modify the pump beam shape, to mimic the pump reshaping that matches the best squeezing generation condition described in Chapter 6; or modify the LO to match the squeezed vacuum mode. We applied several phase images onto the SLM to generate different shapes of the beam. A feedback of the squeezing amount detected by the spectrum analyzer is read by the computer for optimization of the phase mask.

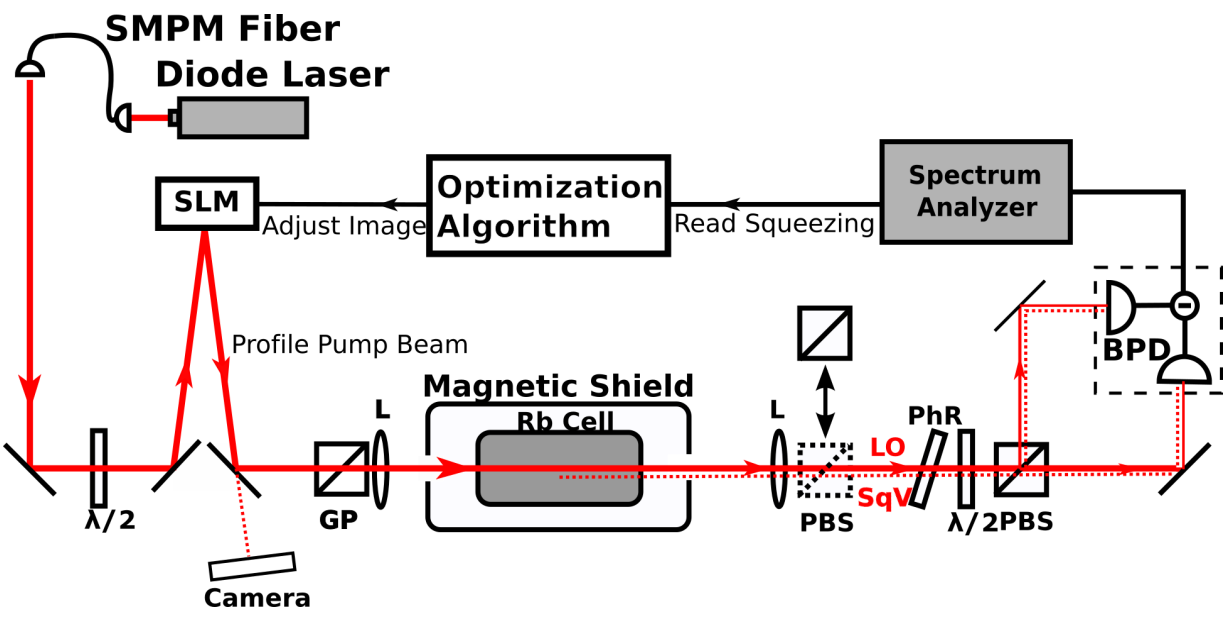

FIG. 7.1: In this setup we put the SLM before the cell, so that we can place a designated phase mask onto the incoming beam, which serves as the pump beam that generates the squeezed field. The spatial profile of the modified beam can be observed at the camera. Meanwhile the squeezing generated in this beam is measured at the balanced photodiode detection after the cell. The computer will read the squeezing level in such condition as a feedback signal and decide how to optimize the feedback to the phase mask, depending on the optimization algorithm we assign.

When the SLM is placed before the cell as is shown in Fig. 7.1, we are adjusting the input pump shape. In Chapter 6 we have achieved a maximum amount of squeezing in the setup where we have a new pump field that has been spatially modified by the atoms in the first cell. Ideally we can use the SLM to get the same spatial mode as the "best squeezing pump" and produce the same or better amount of squeezing.

Theoretically we have unlimited possibilities of mode combinations for beam structure. It is unrealistic for us to test all the mode combinations. As we have discussed in Chapter 5, the LG mode is a natural basis for our mode analysis. For simplicity, we applied two kinds of spatial modification to the beam to add several LG_{l0} modes or LG_{0p} modes (denoted as l modes and p modes in our discussion). When we have N modes (other than the LG_{00} mode) in the phase mask, the number of parameters we have in the optimization system is $2N + 1$. The phase mask applied to the beam is

$$\Phi(x, y) = \sum_{i=1}^{N} (c_{Ri} + ic_{Ii})\Phi_i(w, x, y) \tag{7.1}$$

$\Phi(x, y)$ is the phase change on a pixel at coordinate (x, y). w is the waist of beam found by the optimization process, not necessarily same as the real beam waist. c_{iR} and c_{iI} are the real and imaginary part of the coefficient of the ith mode. $\Phi_i(x, y)$ is the phase change in the ith mode.

The optimization algorithm in the feedback loop is the Metropolis algorithm. In this algorithm, when a change in phase mask results in better squeezing, we accept the change. When the change leads to less squeezing, it is still accepted with a probability.

Ideally, if the optimization runs for infinite amount of time, this algorithm can find a global maximum amount of squeezing, rather than stay in a local optimum.

In our experiments we find a few mode compositions that improves the squeezing result compared to the original Gaussian profile beam under different conditions. We demonstrated 3 improved cases below.

Case 1. Atomic density = 9×10^{12} cm^{-3}. Squeezing with unmodified pump beam = -2.0 dB. Improved squeezing = -2.3 dB. Mode composition is shown in Table 7.1. In Fig. 7.2 we present the comparison between the beam with a "flat" phase mask (left) and the beam with the optimized phase mask (right). A "flat" beam mask is when $N = 0$, the phase change is uniform across the beam. The coefficients of the higher-order modes are displayed in Table 7.1, as well as the optimized beam waist.

TABLE 7.1: Optimal Mode Composition with 5 Higher p Modes

$w(m)$	0.00357		
c_{1R}	-0.00144	c_{1I}	0.00131
c_{2R}	0.789	c_{2I}	-0.174
c_{3R}	-0.00101	c_{3I}	0.182
c_{4R}	0.00810	c_{4I}	0.127
c_{5R}	0.0197	c_{5I}	0.0234

Case 2. Atomic density = 1.5×10^{12} cm^{-3}. Original squeezing = -1.0 dB. Improved squeezing = -1.2 dB. Mode composition is shown in Table 7.2.

Case 3. Atomic density = 6×10^{11} cm^{-3}. Original squeezing = -0.7 dB. Improved squeezing = -1.2 dB. Mode composition is shown in Table 7.2.

In the three cases, the best improvement we got is 0.5 dB on top of a -0.7 dB original squeezing at an atomic density lower than optimal. Though the improved absolute value is

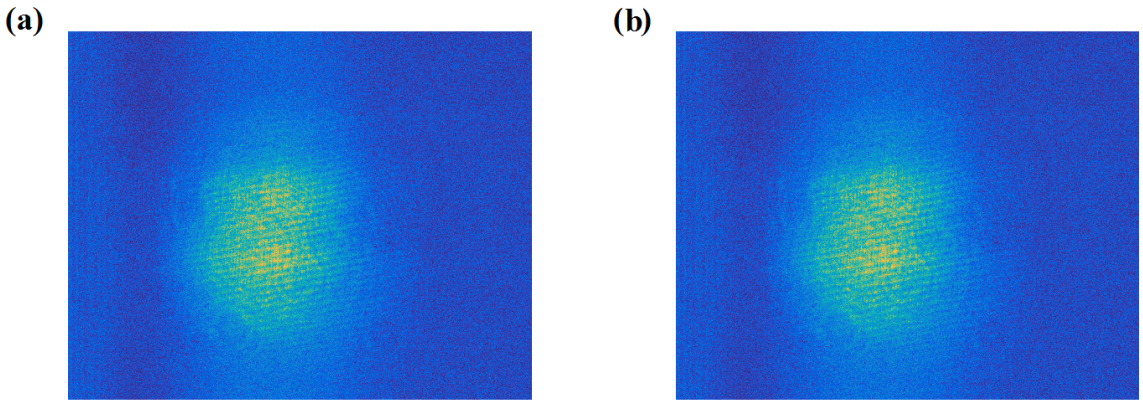

FIG. 7.2: Figure on the left is the "original" beam, with a flat phase mask applied to the SLM. Figure on the right is the "optimized" beam, with the optimal mode composition we find in Case 1.

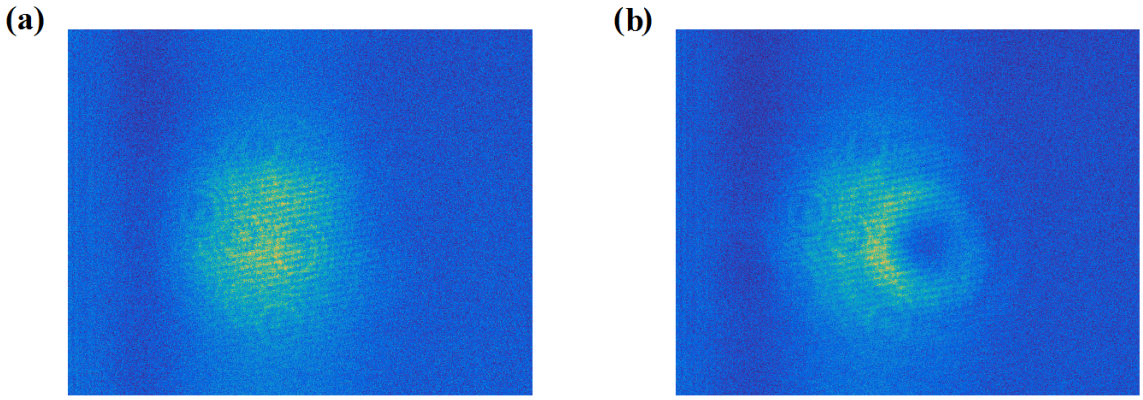

FIG. 7.3: Figure on the left is the "original" beam, with a flat phase mask applied to the SLM. Figure on the right is the "optimized" beam, with the optimal mode composition we find in Case 2.

TABLE 7.2: Optimal Mode Composition with 5 Higher l Modes

$w(m)$	0.00101		
c_{1R}	0.405	c_{1I}	-0.000189
c_{2R}	1.59	c_{2I}	-0.0212
c_{3R}	-0.334	c_{3I}	-0.0395
c_{4R}	1.88	c_{4I}	0.00406
c_{5R}	0.0196	c_{5I}	-0.0120

TABLE 7.3: Optimal Mode Composition with 5 Higher l Modes

$w(m)$	0.00104		
c_{1R}	0.476	c_{1I}	0.0388
c_{2R}	-0.0773	c_{2I}	0.0502
c_{3R}	-0.00768	c_{3I}	-0.00982
c_{4R}	0.0205	c_{4I}	-0.00144
c_{5R}	-0.00368	c_{5I}	-0.00503

not outstanding compared to our best record, it is big progress considering the low atomic density. Furthermore, we see an increase of 0.3 dB at the optimal atomic density in Case 1. This result opened the possibility that we might find a mode composition for the pump beam at this density that produces -2.7 dB as we did in Chapter 6. The possible reason we have not yet achieved -2.7 dB might be that the SLM produces only phase modulation. This is not a "real" beam mode change.

Reshape of the LO

While the pump beam have unlimited amount of possibilities of mode composition. The LO is easier to match since we have some theoretical predictions on its compositions in Chapter 5. Here we place the SLM after the squeezing cell (shown in Fig 7.5) and align it such that the affected polarization is the LO and squeezed field is untouched. We already know that the squeezed vacuum should be in a multu-mode structure of some higher order

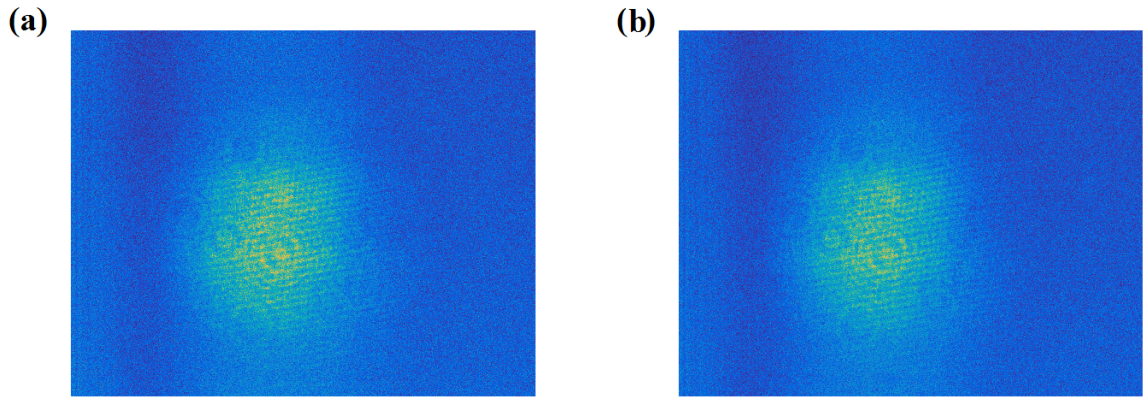

FIG. 7.4: Figure on the left is the "original" beam, with a flat phase mask applied to the SLM. Figure on the right is the "optimized" beam, with the optimal mode composition we find in Case 3.

p modes, we will apply such phase mask to the LO to modify the p mode structure.

However, in such setup we are not able to get improved squeezing. If we bypass the SLM with reflecting mirrors, we can see a noise suppression of -1.8 dB at optimal atomic density. As soon as the SLM is installed, the squeezing becomes -1.0 dB even when a "flat" mask is projected. An assumption of why the squeezing gets degraded is, the liquid crystalls in the SLM screen are slightly oscillating when there voltage is applied. Such oscillation becomes a fluctuation in the phase distribution of the mask, therefore changes the detected noise. This setup would not work for us before we can resolve the liquid crystal oscillation effect.

7.2 Summary

While we know how the spatial mode of the pump field can affect the squeezing, we utilize a feedback loop to change pump beam shape and optimize squeezing. We find a few

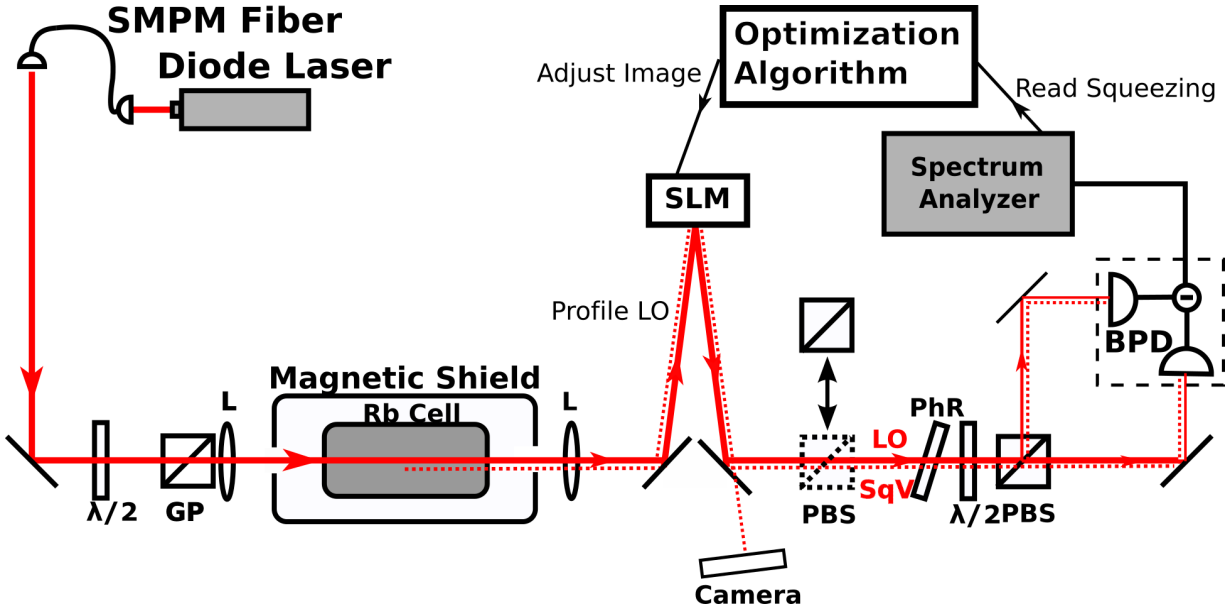

FIG. 7.5: Similarly, we can place the SLM after the cell, the polarization of the outcoming beam has been adjusted so that the SLM will only change the spatial profile of the Local Oscillator. The feedback loop is same as the previous case.

mode compositions of the pump field that can improve the noise suppression. However, the reshape of LO and squeezed field with SLM degrades the detected squeezing, and we believe this results from the configuration of the SLM screen.

CHAPTER 8

Observation of the Spatial Structure

We cannot observe the squeezed beam directly with "normal" cameras when the environmental noise and the dark noise in the camera itself surpasses the beam photon counts. We utilize a quantum noise limited camera with sensors sitting in ultra low temperature environment to reduce the thermal noise and the electronic noise.

8.1 Camera configuration

The camera we utilize is from Princeton Instruments PIXIS series. This camera in our experiments has 1024 $\times$ 1024 pixels on its screen. Each pixel can see photon counts of as low as a few hundred in a short exposure time. Each count of pixel shown in the camera corresponds to four photons incident on the pixel.

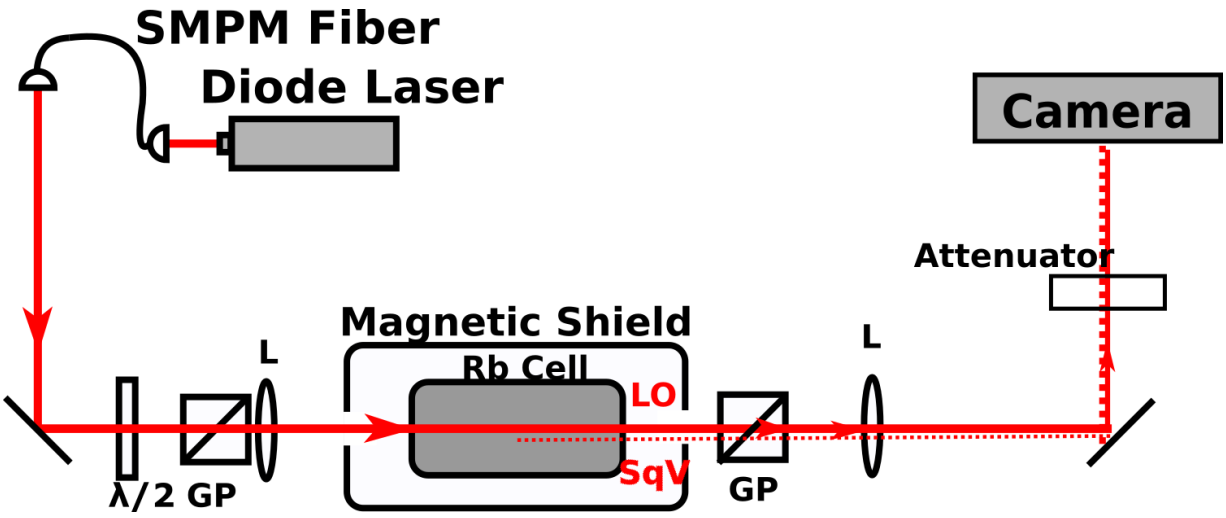

FIG. 8.1: The camera is placed after the cell. The polarizer is used to adjust the polarization we are observing. Attenuator is the neutral density filters we use to attenuate the beam intensity, the strength of attenuation depends on the beam intensity.

8.2 Noise detection

Assume we have a serial of images of a coherent beam taken in a relatively short amount of time under same condition. The average photon number on each pixel is $\overline{N}$ and variance is ΔN^2. The averaged intensity of the beam is plotted in Fig 8.2(a). In Fig 8.2(b), we show the normalized noise of beam $\beta = \overline{N}/\Delta N^2$. For totally random distribution of photon fluctuation in a coherent beam, we know that the variance equals the average of the photon number.

$$\Delta N^2 = \overline{N} \tag{8.1}$$

Theoretically we should see a flat normalized noise image for wherever there is intensity, as is shown in Fig. 8.2(b). In Fig. 8.2(c) we show the statistics of the number variance ΔN^2 vs. the photon counts$\overline{N}$. There are three lines plotted in the figure. The "expected SNL" represents the theoretical shot noise, where $\beta = 1$. The "data run" is a fitting result

of our data, with some low-frequency noise removed in a high-pass filter. Theoretically the noise in the coherent beam should be of same level with the shot noise, but in the figure we see that the noise in the coherent beam is lower than shot noise. This is because we have removed the low-frequency noise in the coherent beam data and reduced the total noise level. In this condition, the theoretical shot noise is no longer a good criteria. Since the dependence of photon variance on photon counts is linear, we would use this fitted line as our "new shot noise", which is shown in "calibrated SNL".

By definition, we know that for a beam with quantum noise manipulated (such as our squeezed vacuum field), the beam intensity fluctuation no longer has such proportionality. The noise distribution will be determined by the squeezing parameter and the phase angle. In Chapter 5 we discussed the spatial structure of the squeezed vacuum and figured out that it is in a combination of higher LG modes. If we observe the statistics of the squeezed vacuum field, the ring structure of the high order LG modes can be observed.

8.2.1 Noise image vs. atomic density

Strong field observation

Before processing the squeezed vacuum field, we observe the LO first since it has a higher intensity and comparatively less environmental disturbance. When we slowly increase the atomic density in the cell and look at the strong field on the camera, we expect the beam to be reshaped, but the noise distribution should always be similar to the coherent beam. The beam image collection is shown in Fig. 8.3.

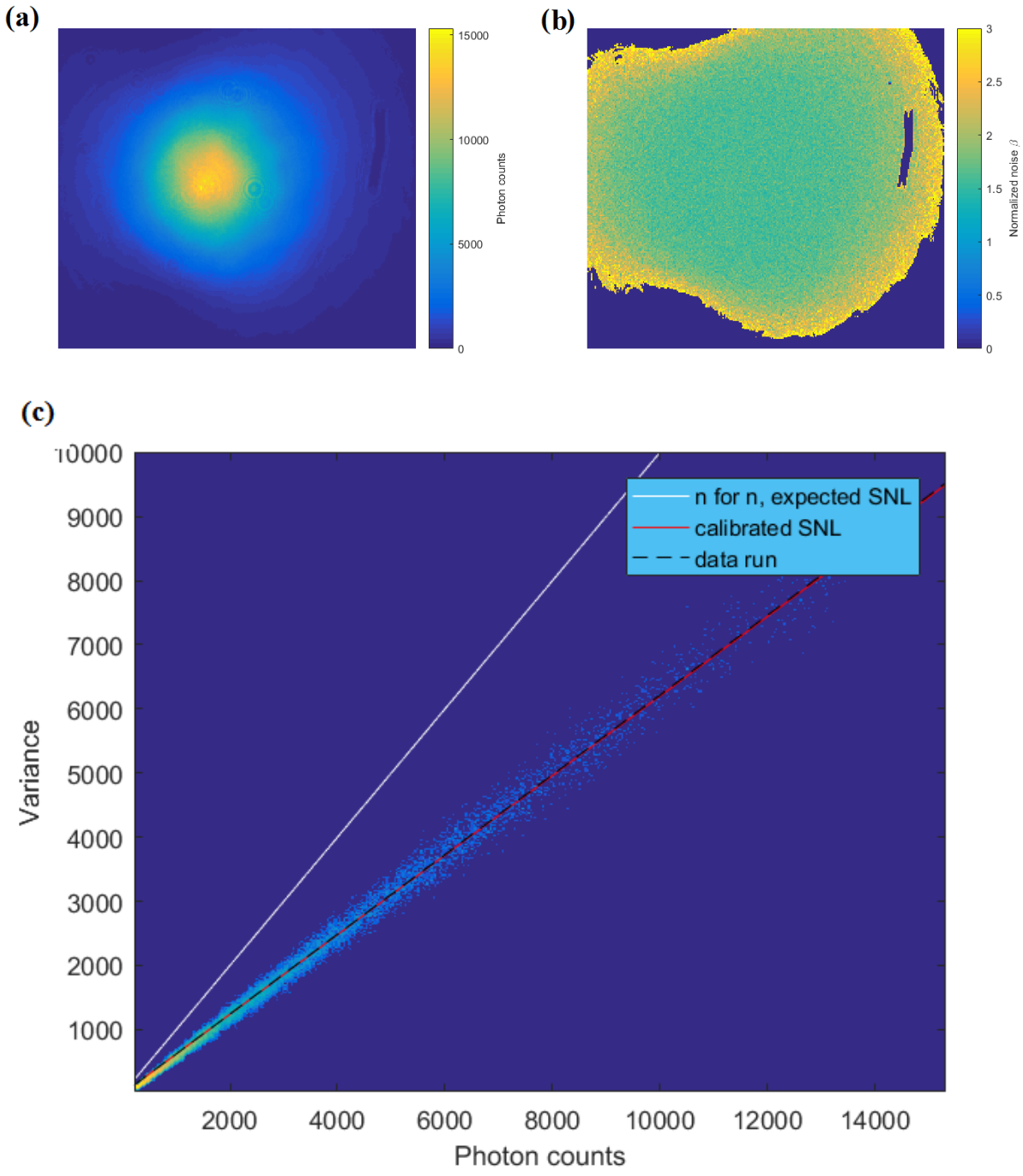

FIG. 8.2: Example of the average intensity (a), normalized noise β (b) and the statistics of the strong field (c). Image (c) is also a heat map, the color of it shows how many data points fall in the designated area.

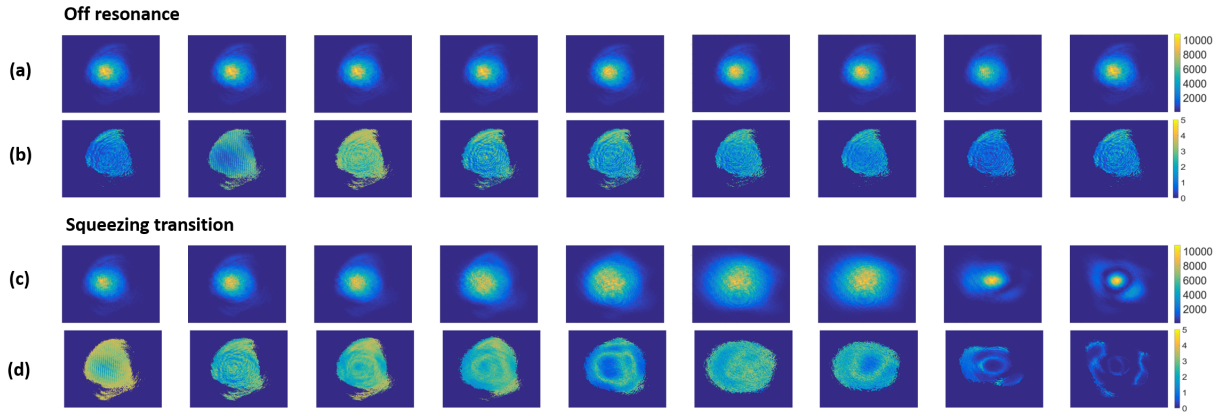

FIG. 8.3: The atomic density of the medium increases from 1.4×10^{10} cm^{-3} to 1.1×10^{13} cm^{-3} from left to right. Top two rows are the averaged intensity (a) and normalized noise map (b) of LO beams when the laser is off resonance. Bottom two rows are the averaged intensity (c) and normalized noise map (d) of LO beams when the laser is tuned to the squeezing detuning.

In Fig 8.3, we have the laser at two different detunings, one is off-resonance and the other is on our squeezing detuning (2 to 2 transition of ^{87}Rb D1 line). While the beam is off resonance, the beam image does not change along with the atomic density. This is a quite straightforward observation in the first row of Fig. 8.3. In contrast, when the laser is tuned on resonance, the beam expands a lot as the atomic density increases, and finally result in a ring structure. Meanwhile in the noise ratio map, we see the same trend that the off-resonance beam does not vary in dependence of the atomic density, and the on-resonance case has the reshaping process.

Squeezed vacuum observation

We observe the squeezed field with the polarizer rotated to a direction so that a minimum amount of light can pass.

In Fig. 8.4, we show that at low atomic densities, the vacuum field is not affected

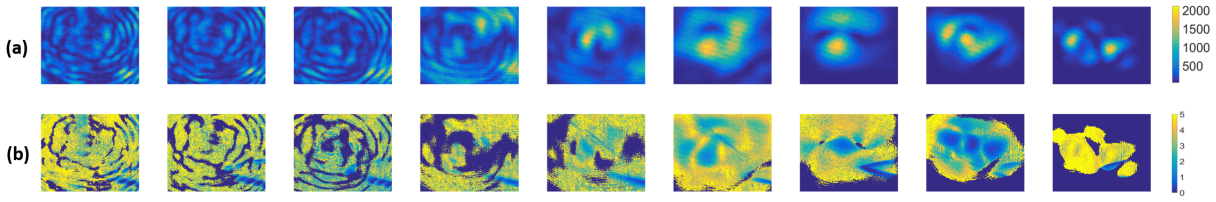

FIG. 8.4: The atomic density of the medium increases from 1.4×10^{10} cm^{-3} to 1.1×10^{13} cm^{-3} from left to right. Row (a) shows the averaged intensity of squeezed field. Row (b) shows the normalized noise β map of squeezed field.

by the atoms at all. As temperature goes up, a more and more pronounced beam shape in this vacuum field is observed. Simultaneously the noise map also starts to illustrate a spatial structure. Among these atomic densities, we focus on the one that produces most squeezing and look at the squeezed field generated in it as shown in Fig. 8.5. Here, in the intensity plot and noise plot, a ring structure is observed as a prediction described in Chapter 5. In the statistics plot (Fig. 8.5) (c), a trident of the slope is observed, indicating that the noise in different spatial areas of a beam has different values. This is the spatial structure of noise we have been looking for. The "calibrated SNL" is the new shot noise we achieve in Fig. 8.2. More of this project will be carried out in the future.

8.3 Summary

With a low-noise camera, we are able to observe the spatial distribution of light noise in the beam. We detect the beam structure directly by analyzing the spatial distribution of photon counts and variance. Due to the low framing rate and thus coupling of light field noise, the normalized noise level we detect in a coherent beam is not on the theoretical shot noise level. Using the noise in a coherent beam as the new "shot noise", we carry out

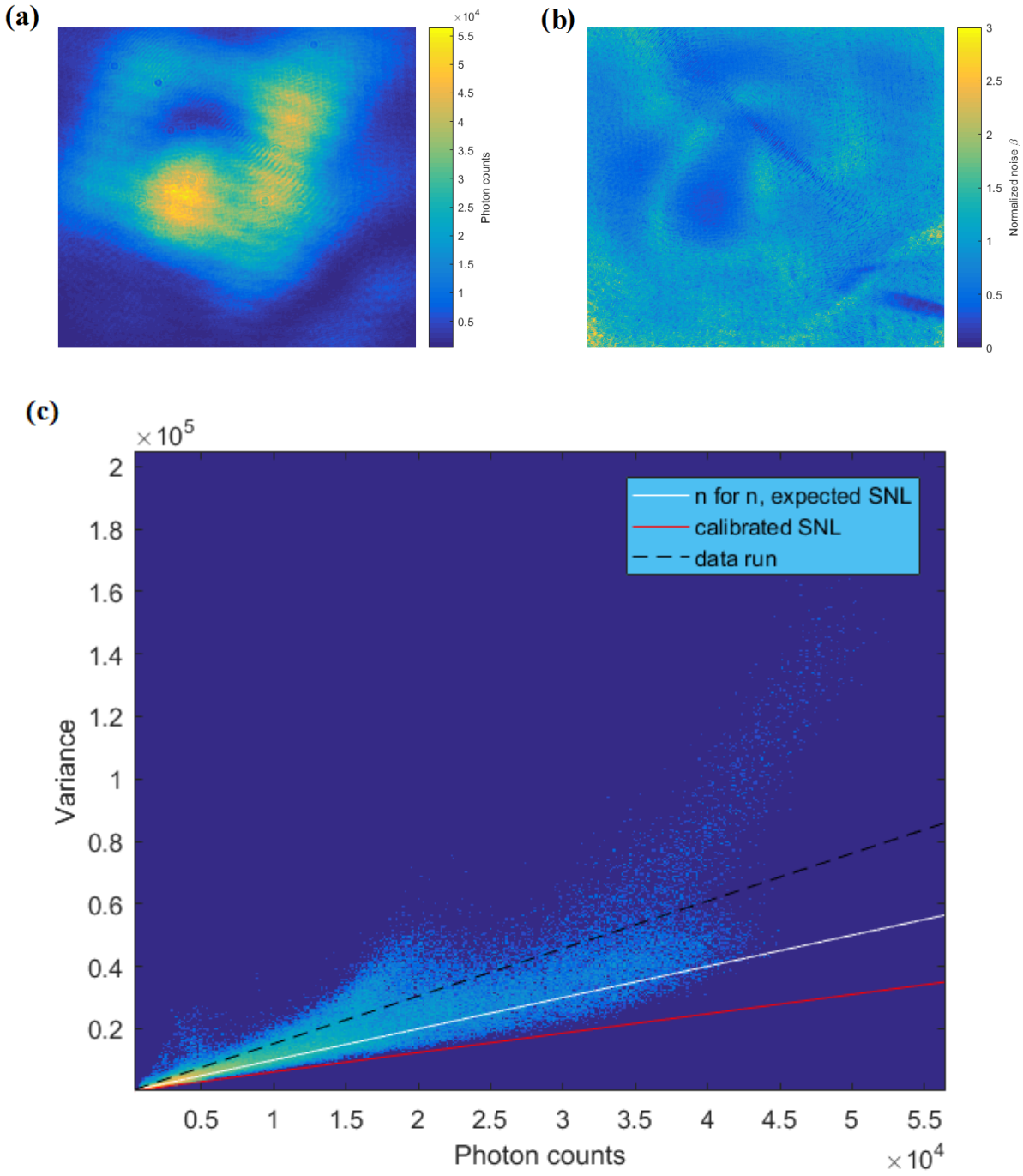

FIG. 8.5: Image of the average intensity (a), fluctuation over intensity (b) and the statistics (c) of the squeezed vacuum field at atomic density = 9.3×10^{11} cm^{-3}. The color of the heat map (c) shows how many data points fall in the designated area.

noise analysis for both LO and squeezed field after the beam interacts with atoms. The noise map of squeezed field exhibits a spatial dependence, which is consistent with our observation in the squeezing measurements.

CHAPTER 9

Conclusion and Outlook

We have achieved a noise suppression of -2.8 dB below the quantum noise limit in a multi-pass of the laser beam through a ^{87}Rb atomic vapor utilizing the PSR effect. We study the factors that affect the noise suppression levels and optimize the possible parameters, such as the atomic density, the pump beam intensity, the spatial profile of the pump beam, etc.

One of these factors is the spatial mode of the pump beam. Contrary to our intuitions, the fluctuation distribution in the beam is not uniform, i.e. proportional to the intensity distribution of the pump beam. We observe the influences of several spatial masks on the squeezing level and concluded that the generated squeezed vacuum is in a multi-mode spatial structure. These Laguerre-Gaussian modes of the squeezed vacuum field largely degrade the noise suppression we measure due to the superposition of the different squeezing angles and parameters from higher modes.

To eliminate the bad mode-match resulting from such multi-mode structure, we build a multi-pass setup. We reduce the atom density but keep the optical depth at about the same level by propagating the beam through the medium several times. However in such a setup the optimization becomes extremely complicated given the complicated nature of the beam focus positions. When we place an identical atomic cell in the system, we find that the best squeezing can be achieved when we reject the squeezed vacuum produced in the first cell and use the modified beam as the new pump.

In the final part of this project, we observe and manipulate the spatial structure of the beam. We are able to pre-program the transverse phase profile of the pump beam or the local oscillator with a spatial light modulator to get a better mode match, therefore improve the squeezing result. Also, by directly looking at the photon counts and variance of it, we observe a spatial dependence of the noise in both LO and squeezed beam.

There are several avenues for further research on the spatial structure of the squeezed field. Our theory collaborators from Louisiana State University are working on explaining why the SLM degrades squeezing as is described in Chapter 7. Study of the SLM structure and how it affects the incident beam will be helpful on reshaping the LO. Our group is also conducting more measurements on the quantum noise limited image to study the structure of the squeezed vacuum field.

BIBLIOGRAPHY

[1] D. F. Walls *et al.*, Nature **306**, 141 (1983).

[2] C. M. Caves and B. L. Schumaker, Phys. Rev. A **31**, 3068 (1985).

[3] R. E. Slusher, L. W. Hollberg, B. Yurke, J. C. Mertz, and J. F. Valley, Phys. Rev. Lett. **55**, 2409 (1985).

[4] M. D. Levenson, R. M. Shelby, A. Aspect, M. Reid, and D. F. Walls, Phys. Rev. A **32**, 1550 (1985).

[5] R. M. Shelby, M. D. Levenson, D. F. Walls, A. Aspect, and G. J. Milburn, Phys. Rev. A **33**, 4008 (1986).

[6] G. J. Milburn, M. D. Levenson, R. M. Shelby, S. H. Perlmutter, R. G. DeVoe, and D. F. Walls, J. Opt. Soc. Am. B **4**, 1476 (1987).

[7] L.-A. Wu, H. J. Kimble, J. L. Hall, and H. Wu, Phys. Rev. Lett. **57**, 2520 (1986).

[8] L.-A. Wu, M. Xiao, and H. J. Kimble, J. Opt. Soc. Am. B **4**, 1465 (1987).

[9] C. K. Hong, Z. Y. Ou, and L. Mandel, Phys. Rev. Lett. **59**, 2044 (1987).

[10] M. Xiao, L.-A. Wu, and H. J. Kimble, Phys. Rev. Lett. **59**, 278 (1987).

[11] H. Vahlbruch, M. Mehmet, K. Danzmann, and R. Schnabel, Phys. Rev. Lett. **117**, 110801 (2016).

[12] H. A. Haus and Y. Yamamoto, Phys. Rev. A **34**, 270 (1986).

[13] S. Machida, Y. Yamamoto, and Y. Itaya, Phys. Rev. Lett. **58**, 1000 (1987).

[14] A. B. Matsko, I. Novikova, G. R. Welch, D. Budker, D. F. Kimball, and S. M. Rochester, Phys. Rev. A **66**, 043815 (2002).

[15] I. Novikova, A. B. Matsko, and G. R. Welch, Journal of Modern Optics **49**, 2565 (2002).

[16] J. Ries, B. Brezger, and A. I. Lvovsky, Phys. Rev. A **68**, 025801 (2003).

[17] E. E. Mikhailov and I. Novikova, Opt. Lett. **33**, 1213 (2008).

[18] S. Barreiro, P. Valente, H. Failache, and A. Lezama, Phys. Rev. A **84**, 033851 (2011).

[19] I. H. Agha, G. Messin, and P. Grangier, Opt. Express **18**, 4198 (2010).

[20] T. Horrom, R. Singh, J. P. Dowling, and E. E. Mikhailov, Phys. Rev. A **86**, 023803 (2012), arXiv:1202.3831 .

[21] L. A. Lugiato and A. Gatti, Phys. Rev. Lett. **70**, 3868 (1993).

[22] A. M. Marino, V. Boyer, R. C. Pooser, P. D. Lett, K. Lemons, and K. M. Jones, Phys. Rev. Lett. **101**, 093602 (2008).

[23] A. Marino, J. Clark, Q. Glorieux, and P. Lett, The European Physical Journal D **66**, 288 (2012), 10.1140/epjd/e2012-30037-1.

[24] M. W. Holtfrerich and A. M. Marino, Phys. Rev. A **93**, 063821 (2016).

[25] G. M. Harry and the LIGO Scientific Collaboration, Classical and Quantum Gravity **27**, 084006 (2010).

[26] E. G. Oelker, *Squeezed states for advanced gravitational wave detectors*, Ph.D. thesis, Massachusetts Institute of Technology (2016).

[27] F. Wolfgramm, A. Cerè, F. A. Beduini, A. Predojević, M. Koschorreck, and M. W. Mitchell, Phys. Rev. Lett. **105**, 053601 (2010).

[28] W. Wasilewski, K. Jensen, H. Krauter, J. J. Renema, M. V. Balabas, and E. S. Polzik, Phys. Rev. Lett. **104**, 133601 (2010).

[29] E. S. Polzik, J. Carri, and H. J. Kimble, Phys. Rev. Lett. **68**, 3020 (1992).

[30] A. I. Lvovsky and M. G. Raymer, Rev. Mod. Phys. **81**, 299 (2009).

[31] Z. Y. Ou, S. F. Pereira, H. J. Kimble, and K. C. Peng, Phys. Rev. Lett. **68**, 3663 (1992).

[32] L.-M. Duan, M. D. Lukin, J. I. Cirac, and P. Zoller, Nature **414**, 413 (2001).

[33] M. D. Lukin, Reviews of Modern Physics **75**, 457 (2003).

[34] H. J. Kimble, Nature **453**, 1023 (2008).

[35] K. Hammerer, A. S. Sørensen, and E. S. Polzik, Rev. Mod. Phys. **82**, 1041 (2010).

[36] A. Furusawa, J. L. Sørensen, S. L. Braunstein, C. A. Fuchs, H. J. Kimble, and E. S. Polzik, Science **282**, 706 (1998).

[37] H.-A. Bachor and T. C. Ralph, *A Guide to Experiments in Quantum Optics*, 2nd ed. (Wiley-VCH, USA, 2004).

[38] D. Budker and D. F. J. Kimball, eds., *Optical Magnetometry* (Cambridge University Press, Cambridge, UK, 2013).

[39] J. Vanier., Applied Physics B: Lasers and Optics **81**, 421 (2005).

[40] M. A. Taylor, J. Janousek, V. Daria, J. Knittel, B. Hage, H.-A. Bachor, and W. P. Bowen, Phys. Rev. X **4**, 011017 (2014).

[41] N. Otterstrom, R. Pooser, and B. Lawrie, Optics Letters **39**, 6533 (2014), arXiv:1409.2935 .

[42] D. A. Steck, (2010).

[43] T. S. Horrom, *Experimental Generation and Manipulation of Quantum Squeezed Vacuum via Polarization Self-Rotation in Rb Vapor*, Ph.D. thesis, College of William and Mary (2013).

[44] E. E. Mikhailov, A. Lezama, T. W. Noel, and I. Novikova, Journal of Modern Optics **56**, 1985 (2009).

[45] D. Grischkowsky and J. A. Armstrong, Phys. Rev. A **6**, 1566 (1972).

[46] J. E. Bjorkholm and A. A. Ashkin, Phys. Rev. Lett. **32**, 129 (1974).

[47] M. Zhang, J. Soultanis, I. Novikova, and E. E. Mikhailov, Opt. Lett. **38**, 4833 (2013).

[48] S. T. Ho, N. C. Wong, and J. H. Shapiro, Opt. Lett. **16**, 840 (1991).

[49] E. E. Mikhailov, A. Lezama, T. W. Noel, and I. Novikova, Journal of Modern Optics **56**, 1985 (2009), arXiv:0903.3156 .

[50] C. F. McCormick, A. M. Marino, V. Boyer, and P. D. Lett, Phys. Rev. A **78**, 043816 (2008).

[51] N. B. Phillips, A. V. Gorshkov, and I. Novikova, Phys. Rev. A **83**, 063823 (2011).

[52] M. Zhang, R. N. Lanning, Z. Xiao, J. P. Dowling, I. Novikova, and E. E. Mikhailov, Phys. Rev. A **93**, 013853 (2016).

[53] A. M. Marino, V. Boyer, R. C. Pooser, P. D. Lett, K. Lemons, and K. M. Jones, Phys. Rev. Lett. **101**, 093602 (2008).

[54] A. Lezama, P. Valente, H. Failache, M. Martinelli, and P. Nussenzveig, Phys. Rev. A **77**, 013806 (2008).

[55] N. V. Corzo, A. M. Marino, K. M. Jones, and P. D. Lett, Phys. Rev. Lett. **109**, 043602 (2012).

[56] G. Barton, *Elements of Green's Functions and Propagation* (Oxford University Press, New York NY, 1989).

[57] R. W. Boyd, *Nonlinear Optics* (Academic Press, 2003) pp. 2,208.

[58] A. Siegman, *Lasers* (University Science Books, Sausalito CA, 1986) pp. 103,647.

[59] P. D. Drummond and Z. Ficek, *Quantum Squeezing* (Springer-Verlag Berlin Heidelberg, 2004) p. 56.

[60] C. Gerry and P. Knight, *Introductory Quantum Optics* (Cambridge University Press, 2005) pp. 152,153.

[61] X. Ma and W. Rhodes, Phys. Rev. A **41**, 4625 (1990).

[62] R. S. Bennink and R. W. Boyd, Phys. Rev. A **66**, 053815 (2002).

[63] T. Horrom, A. Lezama, S. Balik, M. D. Havey, and E. E. Mikhailov, Journal of Modern Optics **58**, 1936 (2011), arXiv:1103.1546 .

[64] M. D. Lukin, M. Fleischhauer, A. S. Zibrov, H. G. Robinson, V. L. Velichansky, L. Hollberg, and M. O. Scully, Phys. Rev. Lett. **79**, 2959 (1997).

[65] R. Wynands and A. Nagel, Appl. Phys. B **68**, 1 (1999).

[66] V. Boyer, A. M. Marino, and P. D. Lett, Phys. Rev. Lett. **100**, 143601 (2008).

[67] V. Boyer, A. M. Marino, R. C. Pooser, and P. D. Lett, Science **321**, 544 (2008).

[68] W. Wasilewski, T. Fernholz, K. Jensen, L. S. Madsen, H. Krauter, C. Muschik, and E. S. Polzik, Opt. Express **17**, 14444 (2009).

[69] R. N. Lanning, Z. Xiao, I. N. Mi Zhang, E. Mikhailov, and J. P. Dowling, (2017), arXiv:1702.01095 .

[70] A. Forbes, A. Dudley, and M. McLaren, Adv. Opt. Photon. **8**, 200 (2016).

[71] N. Matsumoto, T. Ando, T. Inoue, Y. Ohtake, N. Fukuchi, and T. Hara, J. Opt. Soc. Am. A **25**, 1642 (2008).

[72] Y. Ohtake, T. Ando, N. Fukuchi, N. Matsumoto, H. Ito, and T. Hara, Opt. Lett. **32**, 1411 (2007).

[73] B. Sephton, A. Dudley, and A. Forbes, Appl. Opt. **55**, 7830 (2016).